

Multi-view confocal microscopy enables multiple organ and whole organism live-imaging

Olivier Leroy^{1*}, Eric van Leen^{1*}, Philippe Girard^{2‡}, Aurélien Villedieu¹, Christian Hubert³, Floris Bosveld¹, Yohanns Bellaïche^{1‡}, Olivier Renaud^{1‡}

1: Institut Curie, Université PSL, Sorbonne Université, CNRS UMR3215, Inserm U934, Genetics and Developmental Biology, 75005 Paris, France

2: Université de Paris, CNRS, Institut Jacques Monod and Faculty of Basic and Biomedical Sciences, 75006, Paris, France

3: Errol Laser, Saint Maur des Fossés, France

* these authors contributed equally

‡ to whom correspondence should be addressed: olivier.renaud@curie.fr; yohanns.bellaiche@curie.fr; philippe.girard@ijm.fr

Abstract

Understanding how development is coordinated in multiple tissues and gives rise to fully functional organs or whole organisms necessitates microscopy tools. Over the last decade numerous advances have been made in live-imaging, enabling high resolution imaging of whole organisms at cellular resolution. Yet, these advances mainly rely on mounting the specimen in agarose or aqueous solutions, precluding imaging of organisms whose oxygen uptake depends on ventilation. Here, we implemented a multi-view multi-scale microscopy strategy based on confocal spinning disk microscopy, called Multi-View confocal microScopy (MuViScopy). MuViScopy enables live-imaging of multiple organs with cellular resolution using sample rotation and confocal imaging without the need of sample embedding. We illustrate the capacity of MuViScopy by live-imaging *Drosophila melanogaster* pupal development throughout metamorphosis, highlighting how internal organs are formed and multiple organ development is coordinated. We foresee that MuViScopy will open the path to better understand developmental processes at the whole organism scale in living systems that necessitates gas exchange by ventilation.

Introduction

The size, shape and organization of organs, tissues or cells are highly regulated during development, homeostasis and repair. As such, capturing cell, tissue and organ growth and morphogenesis over long periods of time, is central to understand these biological phenomena and to probe their underlying genetic and biophysical regulations (Collinet and Lecuit, 2021; Goodwin and Nelson, 2021; Hannezo and

Heisenberg, 2019). Importantly, cell, tissue or organ dynamics can be driven by long range mechanical coupling, as well as systemic hormonal regulation (Barresi and Gilbert, 2019; Boulan et al., 2015; Cole et al., 2019; Villedieu et al., 2020), highlighting that the understanding of growth and morphogenesis also necessitates cellular imaging of multiple tissues or organs in whole living organisms.

Fluorescent light-microscopy has emerged as an essential technology to study biological systems by live imaging at spatiotemporal resolutions ranging from subcellular to whole organism scale (Keller, 2013). This is best illustrated by two distinct imaging approaches: confocal microscopy and light-sheet microscopy (Fig. 1A) (Bayguinov et al., 2018; Keller and Stelzer, 2008; Keller et al., 2008; Oreopoulos et al., 2014; Wan et al., 2019). Confocal fluorescence microscopes are currently the most commonly used imaging systems with optical sectioning capability. In particular, spinning disk confocal microscopy is a mature, commercially available technology for studying development, homeostasis and repair by live imaging. It can resolve biological processes from the subcellular to the whole-tissue scale. Furthermore, spinning disk confocal microscopy has many advantages over laser scanning confocal microscopy for dynamic imaging, particularly in terms of acquisition speed, photobleaching and phototoxicity (Oreopoulos et al., 2014; Wang et al., 2005). Spinning disk confocal microscopy samples are often mounted on glass slides or specific dishes, where observation is only possible from one side, namely perpendicular to the slide. For many applications in biology, and in particular in the field of developmental biology, it is critical to be able to obtain multiple views of the structure(s) under investigation. Indeed, the observed tissues are often not organized in a uniform layer but present complex 3D structures. In confocal microscopy at the level of individual cells, attempts have been made to better orientate cells by inserting single cells into a glass capillary or fixing them to a glass fiber (Bradl et al., 1994; Bruns et al., 2015; Staier et al., 2011). Whether these approaches would allow to perform a multi-view exploration of tissues or organisms while achieving high resolution imaging of multiple tissues remains unexplored. Complementing confocal microscopy, light-sheet fluorescence microscopy (LSFM) combines intrinsic optical sectioning with wide-field detection (Keller, 2013). In contrast to epifluorescence microscopy only a thin slice (usually a few hundred nanometers to a few micrometers) of the sample is illuminated perpendicularly to the direction of observation. This method allows the acquisition of large field of view images in a

single, spatially confined illumination step; offering low photobleaching, low phototoxicity, good signal-to-noise ratio and improved acquisition speed (de Medeiros et al., 2015; Guignard et al., 2020; Huisken, 2004; McDole et al., 2018; Mertz, 2011; Pitrone et al., 2013; Siedentopf and Zsigmondy, 1902; Strnad et al., 2016; Voie et al., 1993). In addition, the majority of light-sheet microscopes enable sample imaging from different points of view using a sample holder mounted on a rotating stage and/or by having multiple lenses to collect light from different angles (Chhetri et al., 2015; Krzic et al., 2012; Schmid et al., 2013; Tomer et al., 2012; Wu et al., 2013). So far, LSFM permits live *in toto* imaging of immersed/embedded samples. However, there are numerous model organisms that cannot be immersed or embedded as their survival depends on oxygen uptake by ventilation. Whether LSFM can be efficiently applied to non-immersed samples has yet to be tested.

As exemplified by numerous past and recent studies, imaging of *Drosophila* pupae without immersion has been key in the exploration of developmental and repair processes and to characterize core and conserved genetic and biophysical mechanisms driving cell differentiation as well as tissue proliferation, shaping and architecture (Aigouy et al., 2010; Arata et al., 2017; Corson et al., 2017; Curran et al., 2017; Diaz-de-la-Loza et al., 2018; Etournay et al., 2015; Founounou et al., 2013; Franz et al., 2018; Gho et al., 1999; Guirao et al., 2015; Lemke and Schnorrer, 2018; Levayer et al., 2015; Mauri et al., 2014; Michel and Dahmann, 2020; Prat-Rojo et al., 2020; Ray et al., 2015; Sarov et al., 2016). In particular, using spinning disk confocal microscopy, many studies have focused on the dynamics of a single tissue including the pupal wing and dorsal thorax (notum) tissues as well as histoblast nests. Yet, and as in most model systems, it remains critical to investigate multiple tissue and organ dynamics to define the underlying genetic and biophysical mechanisms coordinating the development of a whole organism. Here, we initially set out to test LSFM as an imaging approach to begin to explore genetic and mechanical coupling between multiple organs during *Drosophila* pupa development. While we could use LSFM to image non-embedded pupa, LSFM was not optimal for imaging cell and tissue dynamics with sufficient resolution. Consequently, we developed a Multi-View confocal microScope (MuViScope), which enables confocal multi-view imaging of non-immersed samples over time. We illustrate how its multi-view capability enables visualization of the dynamics of multiple organs, which will be instrumental to address

fundamental biological questions related to organismal development, homeostasis and repair.

Results

Imaging the *Drosophila* pupa using LSFM

We set out to image multiple organs during *Drosophila* pupa development, focusing in particular on the wing and the dorsal thorax. In recent years, LSFM emerged as the technique of choice for the *in toto* imaging of organisms (Wan et al., 2019). A known drawback of LSFM is the shadowing caused by absorption, scattering or refraction of light inside the sample (Rohrbach, 2009). Although these stripe artifacts can be found in any light microscope, they are more pronounced in light-sheet based microscopes due to the illumination from the side. Possible solutions to reduce shadowing include scanning illumination and/or multi-view imaging either by sample rotation or by dual-side sample illumination (Baumgart and Kubitscheck, 2012; de Medeiros et al., 2015; Huiskens and Stainier, 2007; Keller et al., 2008). However, for samples of more than a couple of hundred cells, these artifacts can undermine the ability to clearly image certain structures (Baumgart and Kubitscheck, 2012; de Medeiros et al., 2015; Huiskens and Stainier, 2007; Keller et al., 2008). It remains unknown whether or not these artifacts might hinder the imaging of the *Drosophila* pupa. In addition, most commercial LSFM systems available require sample immersion in liquid or embedding in agarose. This potentially poses significant problems for organisms that rely on ventilation for gas exchange. To assess the possibility for light-sheet microscopy to image *Drosophila* pupae, we first opted for the light-sheet Z1 microscope from Carl Zeiss using dual-illumination on the pupal dorsal thorax epithelium labelled by the adherens junction marker Ecad:3xGFP (Fig. 1 and Fig. S1). Upon imaging of 54 hours after pupa formation (hAPF) old pupae immersed in PBS, the image quality was high on the lateral parts of the tissue and a cellular resolution could be obtained (Fig. 1B, B' and Fig. S1). However, our analysis revealed that immersion of the *Drosophila* pupa in PBS stopped their development as exemplified by the mitotic arrest observed as early as 5 min upon immersion in PBS (Movie S1). Since liquid immersion of the pupa precludes live imaging, we then assessed LSFM image quality on the *Drosophila* pupa using the PhaseView ALPHA3 system (PhaseView, France). This system was chosen because its objective,

detection lens and the light sheet alignment can be adapted to non-immersed samples. However, our tests showed that the light sheet did not homogeneously illuminate the tissue when the dorsal thorax was imaged (Fig. 2A). Especially in the medial part of the notum a very low signal was obtained (Fig. 2A, insert). Likewise, when imaging the lateral side of the pupa the wing, legs and eyes were not homogeneously illuminated (Fig. 2B). In summary, these results illustrate that currently available commercial LSFM systems do not produce high quality images in all areas of the dorsal thorax and wing tissues of the *Drosophila* pupa to record its development by time-lapse microscopy.

Imaging the *Drosophila* pupa using the MuViScope

Spinning disk confocal microscopy has often been employed to image individual epithelial tissues in *Drosophila* such as the wing, notum or the abdomen (Aigouy et al., 2010; Arata et al., 2017; Curran et al., 2017; Diaz-de-la-Loza et al., 2018; Etournay et al., 2015; Founounou et al., 2013; Gho et al., 1999; Guirao et al., 2015; Kanca et al., 2014; Keroles et al., 2014; Levayer et al., 2015; Michel and Dahmann, 2020; Prat-Rojo et al., 2020; Ray et al., 2015). Since individual tissues could successfully be imaged using confocal microscopy, we hypothesized that sample rotation along the anterior-posterior (A-P) axis in combination with confocal microscopy could enable the visualization of multiple tissues. Furthermore, we foresaw that increasing the number of optical paths would enable imaging at multiple views at different magnifications. Accordingly, we developed the Multi-View confocal microScope (MuViScope) (Fig. 2C-F, Fig. 3, Fig. S2 and Movie 1).

The system is based on spinning disk illumination where the light source is composed of a fiber laser bench that is connected to the spinning disk head. The laser beam is focused on the sample by means of mirrors, dichroic mirrors, and lenses. The sample is imaged by using two dry long working distance objectives located on opposite sides of the sample. Each objective corresponds to an optical path where the excitation and collection of light is done via the same objective (Fig. 3A, B). The light emitted from the sample is collected by the excitation lens and passed back to the dichroic mirror located in the spinning disk head, which will reflect the light back to the sCMOS camera. The collection of the image via the opposite lens is done in the same way by changing the optical path using a motorized flip mirror (Fig. 3A, B, Movie 1). The sample is placed at the end of a capillary or metal

rod which is held by a capillary holder (Fig. 3C-F). Samples are mounted by either gluing them to the capillary using dental glue (Fig. 3F) or by sticking them to double side tape on a small metal rod with a flattened end (see Materials and Methods and Supplementary Method). The capillary and metal rod fit into a rotating stage that can be precision controlled along the x-y-z- θ axes (Fig. 3C-F, Fig. S2). Temperature and humidity are controlled within an opaque box, which surrounds the sample, sample holder, x-y-z- θ precision stages and objectives.

First, we assessed the ability of the MuViScope to visualize the dorsal thorax and wing tissues in *Drosophila* pupae (see Table S1 for acquisition procedure and settings). When imaged from the dorsal side, lateral structures such as the eyes and medial structures of the midline in the notum were well captured (Fig. 2C). In addition, the eye, legs, wing and wing veins were readily visualized by rotating the pupa 90° (Fig. 2D). These results stand in contrast to the images acquired using the Phaseview microscope, for which the notum and wing tissues of living pupae could not be visualized without shadowing effects (Fig. 2A, C insets, E). Furthermore, 180° sample rotation combined with two optical arms of the MuViScope offers the possibility to switch between distinct objectives enabling the acquisition of the tissue at different magnifications capturing both global and cellular tissue views in the same animal (Fig. 2F, F'). The MuViScope therefore complements LSFM by permitting higher quality live imaging of non-immersed samples.

Whole animal imaging using the MuViScope

We next explored the capability of the MuViScope to image samples using fluorescence and autofluorescence at the animal scale. We first imaged a pharate adult Ecad:3xGFP *Drosophila* pupa over 90° using the 10x objective (Fig. 4A). The resulting images clearly show major structures like the body segments of the head and thorax and the legs, as well as smaller structures such as the folds in the wing, ommatidia in the eyes, and the bristles on the thorax (Fig. 4A). A 3D reconstruction of a pupa at 28 hAPF was assembled by merging and deconvoluting 8 angles taken over 360° (0°, 45°, 90°, 135°, 190°, 235°, 270° and 315°; see Movie S2). Using 40x magnification, we also acquired a high-resolution dataset of the head and thorax of the pupa over 360°. The 3D fusion and reconstruction of this dataset illustrates the capability of the MuViScope to obtain 360° view of the anterior part of the pupa with cellular resolution (Movie S3). To test the MuViScope on other model organisms,

multiple views of an adult *Tribolium* and *Aranea* were obtained. Using only autofluorescence, the legs, body and eyes could be ascertained in an *Aranea* (Fig. 4B). In the α tub1-LifeAct:GFP, EF1 α -nls:GFP transgenic *Tribolium* adult the body segments, legs and antennae were clearly distinguishable (Fig. 4C and Movie 2). In addition, the resolution was high enough to discern small dimples present on the surface of the outer chitin layer (Fig. 4C'). The MuViScope is therefore capable of generating high quality 360° views in different species.

Imaging *Drosophila* pupa development to eclosion

Our next aim was to perform time-lapse live microscopy experiments. Viability was assessed by placing undissected pupae in the MuViScope imaging chamber with the temperature set to 25°C and humidity to 70%. Under these conditions high pupal viability was achieved (viability 90%, $n = 9/10$). Furthermore, pupal viability remained high upon removal of the pupal case (puparium) (viability 90%, $n = 18/20$), mounting with dental glue (viability 85%, $n = 11/13$) or on double-sided tape (viability 90%, $n = 9/10$). We then checked if pupae could be imaged from 0.5 hAPF to eclosion. For this, we used the transgenic hh-DsRed line, which is visible through the puparium and labels the posterior compartment of tissues (Akimoto et al., 2005). When performing 360° imaging using 4-angles (i.e. 90 degrees apart), hh-DsRed signal could be observed on all sides of the pupa (Fig. 5A and Movie 3). We focused mainly on wing development. Labeling of the posterior compartment of the tissue allowed to observe that the wing posterior compartment undergoes a fast and global posterior movement at 11 hAPF and started to undergo extensive twisting at 38 hAPF (Fig. 5A and Movie 3); two morphogenetic events occurring at the time of head eversion and wing folding respectively (Bainbridge and Bownes, 1981). These results show that the imaging conditions ensure high viability, and accordingly enables imaging of the entire pupal development.

Multiple muscle precursors imaging

Mesodermal tissues in the *Drosophila* pupa develop in multiple locations (Dutta et al., 2004; Jährling et al., 2010; Lemke and Schnorrer, 2018; McGurk et al., 2007). However, some mesodermal tissues in *Drosophila* have not been imaged live, because they develop inside the organism at positions for which mounting under a coverslip might be challenging. Especially difficult to image are the lateral and ventral

muscles in the pupal thorax, because the wing and legs respectively prevent placing a coverslip directly on top of the position where the muscles develop. 3-angle (0°, 90°, 180°) imaging was therefore performed to assess the performance of the MuViScope in imaging organs that develop within the *Drosophila* pupa. The striking pattern of dorsal-longitudinal muscles labelled by Mef2>CD8:GFP in the dorsal thorax could be well captured and imaged during development (Fig. 6, Movie 4). An expansion in the A-P direction was visible between 26 hAPF and 50 hAPF, followed by a phase of muscle definition between 50 hAPF and 98 hAPF (Spletter et al., 2018). Moreover, sample rotation enabled the visualization of muscle development laterally and ventrally (Fig. 6, Movie 4). Muscle expansion in the legs was most notable between 26 hAPF and 50 hAPF. This was followed by a refinement of the pattern of muscles from 50 hAPF and 98 hAPF similar to muscle development in the dorsal thorax. These results confirm and extend previous findings (Dutta et al., 2004; Jährling et al., 2010; McGurk et al., 2007; Spletter et al., 2018) and show that MuViScope is a suitable tool to explore the coordination of internal tissue development.

Imaging multiple epithelial organs during development

In many cases, it might be advantageous to image multiple organs in the same animal to explore 1) whether and how genetic or mechanical developmental interplay exists between organs and 2) how systemic regulation coordinates animal scale development. We therefore set out to explore whether MuViScopy could be well suited to visualize multiple epithelial organs in the same animal. As a test case, we set out to characterize the development of both the wing and the dorsal thorax in both wild-type (wt) and *dumpy* (*dpy*) mutant conditions by labelling the tissue using Ecad:3xGFP. The extracellular matrix protein Dpy is known to control morphogenesis in the wing and dorsal thorax by enabling the attachment of the epidermis to the cuticle (Aigouy et al., 2010; Etournay et al., 2015; Metcalfe, 1970; Olguín et al., 2011; Ray et al., 2015). Previous research has shown that loss of Dpy function leads to misshaped wings and the formation of posterior lateral pits and anterior comma like invaginations in the notum (Aigouy et al., 2010; Etournay et al., 2015; Metcalfe, 1970; Olguín et al., 2011; Ray et al., 2015). Yet, the temporal sequence leading to formation of these defects in different organs has not yet been defined in the same

animal using live microscopy. This therefore offers the opportunity to assess the ability of the MuViScope to explore concomitant tissue dynamics in multiple organs. We first visualized wing (lateral view) and dorsal thorax (dorsal view) tissues in *Ecad:3xGFP* pupa over 90° to assess the wt processes at cell and tissue scale using both 10x and 40x imaging (Fig. 7). In line with published results independently described in the wing and the notum (Aigouy et al., 2010; Etournay et al., 2015; Guirao et al., 2015; Ray et al., 2015), the lateral view enables the observations of the hinge contraction at 17 hAPF and the subsequent elongation of the wing blade, whereas in the dorsal view we could observe the flows of thorax cell towards the anterior as well as the morphogenesis of the posterior lateral region of the notum starting at 21.5 hAPF (Fig. 7A,B, Movie 5). We also checked whether 40x MuViScope imaging enables to quantify tissue flows using particle image velocimetry (PIV, Fig. S3 and Movie S4) as well as to perform cell segmentation, tracking and morphometric quantification of cell dynamics in the wing and notum tissues (Fig. S4, S5). We then performed similar movies in *dpy^{OV1}* animals. In *dpy^{OV1}* prior to 17 hAPF before hinge contraction, the distal end of the wing and the dorsal thorax were similarly shaped compared to wt (Fig. 7A-D, green arrowheads). The distal part of the wing was round and no invaginations could be observed in the notum. Starting from 17 hAPF when the hinge started to contract, the distal part of the *dpy^{OV1}* wing started to change its shape while moving towards the hinge. Accordingly, the wing blade failed to elongate as observed in wt tissues (Movie 5, Fig. 7A-D). Using both the lateral and dorsal view we could observe that like the wt tissue, the hinge contraction was followed in the notum by cell flow towards the anterior at 21 hAPF (Movie 5). However, in *dpy^{OV1}* conditions the anterior comma like invaginations started to appear at 25 hAPF and became progressively more visible until 34 hAPF (Movie 5, Fig. 7C, yellow arrowheads). The posterior lateral pits in the notum appeared at 26.5 hAPF (Fig. 7C, red arrowheads). These pits could not be observed in wt tissue (Fig. 7A, yellow and red arrowheads). Together, these results illustrate that the MuViScope can be used to investigate the morphogenetic processes in both wt and mutant animals in multiple organs within the same animal.

Discussion

Here, we implemented an advanced microscopy methodology named MuViScopy based on spinning disk confocal illumination and multidirectional imaging by sample rotation and double-sided illumination/detection. We showed that this methodology can be used to image Arthropods such as *Tribolium*, *Aranea* and *Drosophila*. In particular, we explored the ability to visualize organs and multiple organ development in *Drosophila*. MuViScopy enables high quality automated 360-degree imaging of living biological samples without sample embedding/emersion. Its conventional sample illumination and fluorescence collection by a single objective enables homogeneous sample illumination without the need for post-acquisition image processing to reconstruct one homogeneously illuminated field of view. External organs such as the epidermis are well captured throughout the entire thorax and could be visualized with cellular resolution. Furthermore, MuViScopy permitted live imaging of the morphogenesis of internal organs that are challenging to image due to their location inside the organism. In addition, multidirectional imaging enables the simultaneous visualization of the development of distinct organs with different magnifications of the same sample in wt or mutant animals. MuViScopy therefore opens up a new range of experimental opportunities to better understand how multiple organs develop as well as to explore the genetic, biophysical and systemic regulations that underlie the organ dynamics. We therefore believe that the MuViScope will be advantageous for the study of fundamental biological questions in organisms that rely on ventilation for gas-exchange. Accordingly, we have provided the MuViScope blueprint and detailed technical information to support the dissemination of MuViScope microscopy.

We foresee that MuViScopy and LSFM will be highly complementary to analyze tissue and organ dynamics (Table S2). Basic optical principles explain some of the complementarity to image immersed versus non-immersed samples. The advantage of LSFM imaging is that the acquisition orthogonal to the illumination plane optimizes photon collection from a given illuminated tissue section (Huisken, 2004), providing a benefit in terms of photobleaching and acquisition time as compared to the MuViScope (Bayguinov et al., 2018; Keller and Stelzer, 2008; Keller et al., 2008; Oreopoulos et al., 2014; Wan et al., 2019). However, the orthogonal acquisition of the LSFM is less favorable when imaging in dry conditions. When the sample is not

immersed the mismatch between the air ($n_0 \simeq 1$) and the sample index (n within the range of 1.38 – 1.42) (Tuchin, 2007) is in the order of 0.4. In both LSFM and MuViScopy, this increases the deflection of the light beam as it hits the sample. In the case of LSFM with acquisition orthogonal to the illumination, this generates a z-offset in focal plane that increases as $d \tan(\Delta\theta)$, whereas the z-offset only scales with $d[1 - \cos(\Delta\theta)]$ in the case of MuViScopy (with d the sample depth, $\Delta\theta = \theta_i - \theta_r$ the difference between the angles of incidence θ_i and refraction θ_r with $\theta_r = \arcsin\left(\frac{\sin \theta_i}{n}\right)$ given by the Snell-Descartes law, Fig. S6A). For example, with $n \simeq 1.4$ (the mean value of the refractive index for the tissue), θ_i of 20° and a depth of $50 \mu\text{m}$, the z-offset will be in the order of $5.13 \mu\text{m}$ for the LSFM and $0.26 \mu\text{m}$ for the MuViScope; the LSFM one being above the Nikon 20X/0.45 and 40X/0.6 air objective axial resolution (respectively $5.09 \mu\text{m}$ and $2.86 \mu\text{m}$ for the GFP emission wavelength of 515 nm , Fig. S6B), and the MuViScope one being in the correct range. In brief, this partly explains why in dry condition, LSFM can still resolve the lateral regions relative to the acquisition direction but not the medial regions, while the MuViScope achieves good cellular resolution in the two regions. In both LSFM and MuViScopy, sample rotation enhances the microscope capabilities by increasing resolution for LSFM and enables to reconstruct sample 360° views for both the LSFM and MuViScope.

We see room to improve the MuViScope in multiple ways. First, a sample finder module as is present on the commercial Carl Zeiss Z1 system could reduce the time spent finding the optimal focus. Second, the design of the sample holder was inspired by light-sheet microscopy. This entails that the sample holder currently only fits one pupa. Enlarging the mounting area would increase sample throughput at the cost of reducing the number of angle position that can be imaged. Third, photon collection could be optimized by using a higher quantum efficiency sCMOS camera and a field homogenizer module. Lastly, the addition of new electrically tunable lenses would increase the acquisition speed of the z-stacks by enabling successive z plane imaging without moving the sample. We foresee that these future changes will further enhance the range of applications of the MuViScope in the study of fundamental biological questions.

Materials and Methods

Confocal MuViScope microscope

A schematic outline of the MuViScope microscope (MuViScope) that was created using the 3D modeling software Solidworks (Dassault Systèmes SolidWorks Corporation, Waltham, MA, USA) is shown in Fig. 3. Technical drawings of the MuViScope and custom optical components are shown in Fig. S2. A comprehensive list of MuViScope components is also provided in Fig. S2B. The MuViScope consists of a multi-laser unit (GATACA systems, France), one spinning disk confocal scan head (Yokogawa CSU-W1, Andor Technology) equipped with sCMOS (scientific complementary metal-oxide semiconductor) camera (Orca Flash 4.0 v2, Hamamatsu) and a home-made specimen holder, which is magnetically attached to a four-axis specimen-positioning system (x-y-z- θ). The system was built on an optical anti-vibration table (TMC, USA). The multi-laser bench is equipped with four laser lines 405 nm, 488 nm, 561 nm and 642 nm. The laser beam is guided through a single-mode fiber into the confocal spinning disk head. The optical path between the spinning disk head and the sample consists of two optical arms that direct light into two opposing dry objective lenses (Fig 3A, B, D). Each arm is composed of mirrors, a tube lens (TI-E 1x, Nikon Instruments Inc.) and an objective (CFI Plan Apo Lambda 10X/0.45 or CFI S Plan Fluor ELWD 40X/0.6, Nikon Instruments Inc.).

The collimated beam at the exit of the spinning-disk head is passing through a relay lens system and then diverted into the desired optical arm using a motorized flip mirror (custom-made by Errol Laser). The collected light follows the same optical path and is reflected from this flip mirror back onto the spinning disk head. A dichroic mirror and an internal detection-filter wheel located in the spinning disk head reflect the fluorescence to the camera. The detection-filter wheel contains various detection filters (BrightLine long-pass and band-pass filters, Semrock) for imaging GFP and DsRed fluorophores. The capillaries (or rods) are inserted into a custom specimen holder made of stainless steel and held in place by the use of Teflon glands. The sample holder is then fitted into the axis of the rotating stage using a magnetic adapter. The whole assembly is held tightly and accurately to the four-axis specimen-positioning system (see Fig. 3 and Fig. S1). This four-axis (x-y-z- θ) specimen-positioning system consists of three motorized linear stages (2x M-404.1DG and 1xM-111.1DG, Physik Instrument) and one rotary stage (M-660.55, Physik

Instrument) controlled by a 4-axes motion controller (C-884.4DC, Physik Instrument). With this system, the specimen holder can be translated along three axes and rotated around its main axis. A thermostatically controlled black plexiglass enclosure covers the whole unit. The temperature is controlled by the Cube temperature module (Life Imaging Services, Switzerland), and the humidity by a commercial humidifier (Eva, Stadler Form). These modules include sensors that are placed near the sample and maintain the user-defined temperature and humidity level. A cover at the top of the chamber provides access to the sample holder. A cold light source is available to help for sample positioning using brightfield illumination.

The optomechanical devices of the MuViScope are all operated through Metamorph software (Molecular Devices, version 7.8.13). The motorized flip mirror is controlled by a custom-made controller (Errol Laser, France) via a DAC (digital-to-analog controller).

Drosophila stocks.

Drosophila stocks were maintained on standard food at 25°C. Stocks used: Ecad:3xGFP (Pinheiro et al., 2017), Ecad:GFP (Huang et al., 2009), *dpy*^{OV1} (Bloomington #276), Mef2:GAL4>UAS-CD8:GFP (Mef2>CD8:GFP, gift from F. Schnorrer), hh-DsRed (hh-Pyr215, Kyoto DGGR 109137).

Sample preparation

Drosophila pupae were staged by collecting white pupae (0 hours after puparium formation, hAPF). The puparium was removed for imaging except for the hh-DsRed experiment. Mounting and dissection was done under a binocular (Carl Zeiss). The posterior part of the pupal case was glued either (i) at the end of a capillary as done for other specimens in Laroche et al., 2019 using dental glue (Protemp II RF A3, 3M) for full rotation imaging (Fig. 3F); or (ii) the entire pupa was placed on double-sided tape (D6661933, 3M) on a flat platform at the end of a metal rod. The pupal case was then delicately dissected from the head to the beginning of the abdomen, either completely or only dorsal laterally (Jauffred and Bellaiche, 2012; Zitserman and Roegiers, 2011). The capillary was then installed on its holder and inserted into the rotating stage. Dental glue mounting enabled unconstrained 360° rotation around the

pupa's anterior-posterior axis. A detailed protocol of the sample preparation is available in Supplementary Methods (Material S1).

Tribolium transgenic α tub1-LifeAct:GFP, EF1 α -nls:GFP (van Drongelen et al., 2018) adults were grown at 29°C in a Tupperware container containing flour and yeast. The *Tribolium* was euthanized by placing it at -20°C for 1h. It was then fixed using dental glue to the end of the capillary as detailed above.

Aranea were collected in the wild in Paris (France) and stored in ethanol before imaging. *Aranea* was fixed to the end of the capillary by using dental glue.

All imaging with MuViScope was performed at 25°C.

Evaluation of pupa viability.

Staged *Drosophila* pupae (30 hAPF) were lined up in a petri dish with the basal part on the plastic side. Four conditions were tested: pupae without glue, pupae glued on the ventral side with double-sided tape (3M), pupae glued at their end with dental glue (Protemp II RF A3, 3M), pupa glued at their end with UV activated glue (UHU, EAN:4026700481501). The petri dishes were placed in a box containing wet paper and placed in an incubator at 25°C for 7 days. The number of empty pupae was counted to assess the survival rate. To assess pupal viability upon immersion, staged Ecad:GFP pupae (12 hAPF) were mounted under a coverslip (Bosveld et al., 2012; Gho et al., 1999) and imaged with a 40x oil objective every 5 min on a Nikon CSU-W1 inverted spinning disk microscope fitted with a Hamamatsu Orca Flash 4.0 sCMOS camera and a Borealis module from Andor (Oxford Instruments) for better illumination homogeneity. After 50 minutes 200-400 μ L of PBS was added with a pipette between the slide and the coverslip and images were acquired every 5 min to assess cell and tissue dynamics upon immersion.

Image Acquisition

The Metamorph acquisition software allows total control of the MuViScope via the Multi-acquisition mode. The control of the axes is done in the "Stage" tab of the "Multi Dimension Acquisition" menu (MDA) of the software. We use the Z2 stage function to control the rotating stage. The acquisition mode includes the acquisition of z-stack time-lapse images at multiple angles and the creation of mosaics enabling the acquisition of the entire sample. All of these modalities can be combined depending

on the type of acquisition required (e.g. multi-view tiling with time-lapse). The following parameters of acquisitions are available in the MuViScope control software (Metamorph) in a sequential order: xy coordinate of the image (xy), multi-channel imaging (ch), z-stack (z), multi-positions allowing tiling (P), multi-angles (θ) and two different magnifications (M). In brief, the order of acquisition is as follows: $xy \rightarrow ch \rightarrow z \rightarrow P \rightarrow \theta \rightarrow M \rightarrow t$. For most of the acquisitions, the exposure time per image was 400ms in binning 2 and a laser power of 0.6 mW at 488 nm and 1.5 mW at 561nm measured at the back focal plane of the objectives. For imaging, depending on the sample, a 100-500 μ m z-stack was acquired each time-point at 4 μ m (10x objective) or 2 μ m (40x objective) z-spacing. The rotation speed of the stage is 212°/sec in our experimental conditions. This represents the speed at which the stage can turn from one angle to the next and does not include the time necessary for image acquisition. The time between two acquisitions was either 15min or 30min. The detailed acquisition parameters for each figure are provided in Table S1.

The temperature of the thermostatically controlled chamber was set to 25°C with a humidity level of 70%. Samples were located using transmission light (white LED, Lumiled) and then finely focused using spinning disk confocal imaging by moving the motors in x, y, z, θ via the Metamorph software.

Light-sheet fluorescence microscopy

LSFM was performed using the Lightsheet Z1 microscope (Carl Zeiss; illumination lens 10x/0.2 Carl Zeiss, – detection lens 20X/1.0 W Carl Zeiss) for pupae immersed in PBS and the alpha3 light-sheet microscope system (PhaseView; illumination lens: EPIPLAN 10X/0.23 Carl Zeiss – detection lens MPLN 10X/0.25 Olympus) for pupae without immersion. Pupae were attached to the capillary with dental glue under the same conditions as for the MuViScope (see *Sample preparation*).

Image processing

Time-lapse images and multi-view z-stack acquisitions were processed using Fiji software (Schindelin et al., 2012). Briefly, for each angle and at each time point, a maximum projection (MIP) of z-stack images was made and then, if necessary, the resulting multi-view MIP images were stitched with the Pairwise Stitching plugin (Preibisch et al., 2009). This was done for every angle and every time point. A movie

was then made from the sequential acquisitions and a montage showing the angles side by side was created by using the Stack Combiner plugin (Wayne S. Rasband, 1997). For Fig. 7, the images were denoised using ND-Safir software (Boulanger et al., 2010) and movie 5 was realigned using the ImageJ plugin StackReg (Thévenaz et al., 1998). 3D reconstruction by fusion/deconvolution of multi-angle light-sheet or MuViScopy data were performed using Huygens Fuser software (SVI). The alignment of the different views was first done manually using the interactive Fuser & Decon alignment module then an automatic registration in "full optimization on initial guess" is performed followed by a fusion deconvolution (Huygens Fuser, SVI).

Tissue flow and cell dynamics quantification

Local tissue flows were quantified using movies of pupae expressing Ecad:3xGFP. For each movie, the flow field was obtained by image cross-correlation (IC) velocimetry along sequential images using customized MATLAB routines based (Bosveld et al., 2012; Raffel et al., 2018) on the particle image velocimetry (PIV) toolbox *matpiv* (<http://folk.uio.no/jks/matpiv>). PIV was performed within boxes of 40 square pixels ($\sim 13 \times 13 \mu\text{m}^2$, pixel size $0.32 \mu\text{m}$) with 50% overlap for spatial averaging and integrated over 2 h. Averaging PIV flows from different pupae was done by generating a tissue archetype in order to register and rescale each time-lapse movie. Registration and rescaling were performed using the four dorsocentral macrochaetae as landmarks (Guirao et al., 2015). Each PIV box is then positioned according to the barycenter of the 4 macrochaetae and rescaled. Together, this enables improved comparison of the MuViScope and spinning disk microscope conditions by reducing the spatial dispersion of the landmarks and averaging of PIV measurements.

Segmentation was performed using Imaris software (Oxford Instruments) within the wing or using previously published MATLAB (Mathworks) routines based on standard watershed algorithm within the scutellum (Bosveld et al., 2012; Guirao et al., 2015). Upon segmentation and multiple rounds of manual and automated correction, cells were tracked and cell areas analyzed using previously published MATLAB and C++ routines (Bosveld et al., 2012; Guirao et al., 2015).

Acknowledgements

We would like to thank: Frank Schnorrer (Institute for Developmental Biology Marseille), the Bloomington *Drosophila* stock center and Kyoto stock center for *Drosophila* stocks, Maurijn van der Zee and Kees Koops (both Leiden University) for *Tribolium* stocks, France Lam (Institute of Biology Paris-Seine) for access to and help with the Phaseview Alpha3 system, the cellular imaging platform at SFR Necker for access to the Zeiss Z1 lightsheet microscope and Sébastien Dupichaud for his help in operating it, Maïté Coppey (Institut Jacques Monod) for help with writing funding applications, Christine Rollard (Muséum national d'Histoire naturelle) for help with spider identification, François Graner and Isabelle Bonnet for the fruitful discussions and preliminary tests at the beginning of the project, Aude Maugarny-Calès for her advice and help with *Drosophila* sample mounting and Cyril Kana Tepakbong for help with image analysis. The MuViScope was financed by France-BioImaging national research infrastructure (ANR-10-INBS-04) and additional funding from ERC Advanced (TiMorph, 340784), ARC (SL220130607097), ANR Migrafolids (ANR-18-CE13-0021), ANR Labex DEEP (11-LBX-0044, PSL ANR-10-IDEX-0001-02) grants. EvL was financed by the ITN 'PolarNet' (675407), EvL and AV were both financed by the FRM (FDT201904008163, FDT201805005805).

Competing interests

The authors declare no competing interests

Bibliography

- Aigouy, B., Farhadifar, R., Staple, D. B., Sagner, A., Röper, J.-C., Jülicher, F. and Eaton, S.** (2010). Cell flow reorients the axis of planar polarity in the wing epithelium of *Drosophila*. *Cell* **142**, 773–86.
- Akimoto, A., Wada, H. and Hayashi, S.** (2005). Enhancer trapping with a red fluorescent protein reporter in *Drosophila*. *Dev Dyn* **233**, 993–997.
- Arata, M., Sugimura, K. and Uemura, T.** (2017). Difference in Dachsous Levels between Migrating Cells Coordinates the Direction of Collective Cell Migration. *Dev Cell* **42**, 479–497.e10.
- Bainbridge, S. P. and Bownes, M.** (1981). Staging the metamorphosis of *Drosophila melanogaster*. *Development* **66**, 57–80.
- Barresi, M. J. F. and Gilbert, S. F.** (2019). *Developmental Biology*. 12th edition. Sinauer Associates is an imprint of Oxford University Press.
- Baumgart, E. and Kubitscheck, U.** (2012). Scanned light sheet microscopy with confocal slit detection. *Opt Express* **20**, 21805–21814.

Bayguinov, P. O., Oakley, D. M., Shih, C.-C., Geanon, D. J., Joens, M. S. and Fitzpatrick, J. A. J. (2018). Modern Laser Scanning Confocal Microscopy. *Curr Protoc Cytom* **85**, e39.

Booth, M. J. and Wilson, T. (2001). Refractive-index-mismatch induced aberrations in single-photon and two-photon microscopy and the use of aberration correction. *J Biomed Opt* **6**, 266–272.

Bosveld, F., Bonnet, I., Guirao, B., Tlili, S., Wang, Z., Petitalot, A., Marchand, R., Bardet, P.-L., Marcq, P., Graner, F., et al. (2012). Mechanical Control of Morphogenesis by Fat/Dachsous/Four-Jointed Planar Cell Polarity Pathway. *Science* **336**, 724–727.

Boulan, L., Milán, M. and Léopold, P. (2015). The Systemic Control of Growth. *Cold Spring Harb Perspect Biol* **7**,.

Boulanger, J., Kervrann, C., Bouthemy, P., Elbau, P., Sibarita, J.-B. and Salamero, J. (2010). Patch-based nonlocal functional for denoising fluorescence microscopy image sequences. *IEEE Trans Med Imaging* **29**, 442–454.

Bradl, J., Hausmann, M., Schneider, B., Rinke, B. and Cremer, C. (1994). A versatile 2 π -tilting device for fluorescence microscopes. *Journal of Microscopy* **176**, 211–221.

Bruns, T., Schickinger, S. and Schneckenburger, H. (2015). Sample holder for axial rotation of specimens in 3D microscopy. *Journal of Microscopy* **260**, 30–36.

Chhetri, R. K., Amat, F., Wan, Y., Höckendorf, B., Lemon, W. C. and Keller, P. J. (2015). Whole-animal functional and developmental imaging with isotropic spatial resolution. *Nat Methods* **12**, 1171–1178.

Cole, T. J., Short, K. L. and Hooper, S. B. (2019). The science of steroids. *Semin Fetal Neonatal Med* **24**, 170–175.

Collinet, C. and Lecuit, T. (2021). Programmed and self-organized flow of information during morphogenesis. *Nat Rev Mol Cell Biol* **22**, 245–265.

Corson, F., Couturier, L., Rouault, H., Mazouni, K. and Schweisguth, F. (2017). Self-organized Notch dynamics generate stereotyped sensory organ patterns in *Drosophila*. *Science* **356**,.

Curran, S., Strandkvist, C., Bathmann, J., de Gennes, M., Kabla, A., Salbreux, G. and Baum, B. (2017). Myosin II Controls Junction Fluctuations to Guide Epithelial Tissue Ordering. *Developmental Cell* **43**, 480-492.e6.

de Medeiros, G., Norlin, N., Gunther, S., Albert, M., Panavaite, L., Fiuza, U.-M., Peri, F., Hiriagi, T., Krzic, U. and Hufnagel, L. (2015). Confocal multiview light-sheet microscopy. *Nat Commun* **6**, 8881.

Diaz-de-la-Loza, M.-D.-C., Ray, R. P., Ganguly, P. S., Alt, S., Davis, J. R., Hoppe, A., Tapon, N., Salbreux, G. and Thompson, B. J. (2018). Apical and Basal Matrix Remodeling Control Epithelial Morphogenesis. *Dev Cell* **46**, 23-39.e5.

Dutta, D., Anant, S., Ruiz-Gomez, M., Bate, M. and VijayRaghavan, K. (2004). Founder myoblasts and fibre number during adult myogenesis in *Drosophila*. *Development* **131**, 3761–3772.

Etournay, R., Popović, M., Merkel, M., Nandi, A., Blasse, C., Aigouy, B., Brandl, H., Myers, G., Salbreux, G., Jülicher, F., et al. (2015). Interplay of cell dynamics and epithelial tension during morphogenesis of the *Drosophila* pupal wing. *Elife* **4**, e07090.

- Founounou, N., Loyer, N. and Le Borgne, R.** (2013). Septins regulate the contractility of the actomyosin ring to enable adherens junction remodeling during cytokinesis of epithelial cells. *Dev Cell* **24**, 242–255.
- Franz, A., Wood, W. and Martin, P.** (2018). Fat Body Cells Are Motile and Actively Migrate to Wounds to Drive Repair and Prevent Infection. *Dev Cell* **44**, 460–470.e3.
- Gho, M., Bellaïche, Y. and Schweisguth, F.** (1999). Revisiting the *Drosophila* microchaete lineage: a novel intrinsically asymmetric cell division generates a glial cell. *Development* **126**, 3573–3584.
- Goodwin, K. and Nelson, C. M.** (2021). Mechanics of Development. *Dev Cell* **56**, 240–250.
- Guignard, L., Fiúza, U.-M., Leggio, B., Laussu, J., Faure, E., Michelin, G., Biasuz, K., Hufnagel, L., Malandain, G., Godin, C., et al.** (2020). Contact area-dependent cell communication and the morphological invariance of ascidian embryogenesis. *Science* **369**,.
- Guirao, B., Rigaud, S. U., Bosveld, F., Bailles, A., López-Gay, J., Ishihara, S., Sugimura, K., Graner, F. and Bellaïche, Y.** (2015). Unified quantitative characterization of epithelial tissue development. *eLife* **4**, 1–52.
- Hannezo, E. and Heisenberg, C.-P.** (2019). Mechanochemical Feedback Loops in Development and Disease. *Cell* **178**, 12–25.
- Huang, J., Zhou, W., Dong, W., Watson, A. M. and Hong, Y.** (2009). Directed, efficient, and versatile modifications of the *Drosophila* genome by genomic engineering. *Proc Natl Acad Sci U S A* **106**, 8284–8289.
- Huisken, J.** (2004). Optical Sectioning Deep Inside Live Embryos by Selective Plane Illumination Microscopy. *Science* **305**, 1007–1009.
- Huisken, J. and Stainier, D. Y. R.** (2007). Even fluorescence excitation by multidirectional selective plane illumination microscopy (mSPIM). *Opt Lett* **32**, 2608–2610.
- Jährling, N., Becker, K., Schönbauer, C., Schnorrer, F. and Dodt, H.-U.** (2010). Three-dimensional reconstruction and segmentation of intact *Drosophila* by ultramicroscopy. *Front Syst Neurosci* **4**, 1.
- Jauffred, B. and Bellaïche, Y.** (2012). Analyzing frizzled signaling using fixed and live imaging of the asymmetric cell division of the *Drosophila* sensory organ precursor cell. *Methods in molecular biology (Clifton, N.J.)* **839**, 19–25.
- Kanca, O., Caussinus, E., Denes, A. S., Percival-Smith, A. and Affolter, M.** (2014). Raeppli: a whole-tissue labeling tool for live imaging of *Drosophila* development. *Development* **141**, 472–480.
- Keller, P. J.** (2013). Imaging morphogenesis: technological advances and biological insights. *Science* **340**, 1234168.
- Keller, P. J. and Stelzer, E. H.** (2008). Quantitative in vivo imaging of entire embryos with Digital Scanned Laser Light Sheet Fluorescence Microscopy. *Current Opinion in Neurobiology* **18**, 624–632.
- Keller, P. J., Schmidt, A. D., Wittbrodt, J. and Stelzer, E. H. K.** (2008). Reconstruction of Zebrafish Early Embryonic Development by Scanned Light Sheet Microscopy. *Science* **322**, 1065–1069.
- Keroles, M. B., Dusseault, S. K., Liu, C., Mohammed, M. R., Vadakkan, C. M., Amiel, J. H., Abel, S. N., Bensoussan, E. R., Russell, B. L. and Baker, J.** (2014). Imaging Through the Pupal Case of *Drosophila melanogaster*. *JoVE* 51239.

- Krzic, U., Gunther, S., Saunders, T. E., Streichan, S. J. and Hufnagel, L.** (2012). Multiview light-sheet microscope for rapid in toto imaging. *Nat Methods* **9**, 730–733.
- Laroche, T., Burri, O., Dubey, L. K. and Seitz, A.** (2019). Development of Sample-Adaptable Holders for Lightsheet Microscopy. *Front Neuroanat* **13**, 26.
- Lemke, S. B. and Schnorrer, F.** (2018). In Vivo Imaging of Muscle-tendon Morphogenesis in *Drosophila* Pupae. *J Vis Exp*.
- Levayer, R., Hauert, B. and Moreno, E.** (2015). Cell mixing induced by myc is required for competitive tissue invasion and destruction. *Nature* **524**, 476–480.
- Mauri, F., Reichardt, I., Mummery-Widmer, J. L., Yamazaki, M. and Knoblich, J. A.** (2014). The conserved discs-large binding partner Banderuola regulates asymmetric cell division in *Drosophila*. *Curr Biol* **24**, 1811–1825.
- McDole, K., Guignard, L., Amat, F., Berger, A., Malandain, G., Royer, L. A., Turaga, S. C., Branson, K. and Keller, P. J.** (2018). In Toto Imaging and Reconstruction of Post-Implantation Mouse Development at the Single-Cell Level. *Cell* **175**, 859-876.e33.
- McGurk, L., Morrison, H., Keegan, L. P., Sharpe, J. and O’Connell, M. A.** (2007). Three-Dimensional Imaging of *Drosophila melanogaster*. *PLOS ONE* **2**, e834.
- Mertz, J.** (2011). Optical sectioning microscopy with planar or structured illumination. *Nature Methods* **8**, 811–819.
- Metcalfe, J. A.** (1970). Developmental genetics of thoracic abnormalities of dumpy mutants of *Drosophila melanogaster*. *Genetics* **65**, 627–654.
- Michel, M. and Dahmann, C.** (2020). Tissue mechanical properties modulate cell extrusion in the *Drosophila* abdominal epidermis. *Development* **147**,.
- Olguín, P., Glavic, A. and Mlodzik, M.** (2011). Intertissue mechanical stress affects Frizzled-mediated planar cell polarity in the *Drosophila notum* epidermis. *Curr Biol* **21**, 236–242.
- Oreopoulos, J., Berman, R. and Browne, M.** (2014). Spinning-disk confocal microscopy: present technology and future trends. *Methods Cell Biol* **123**, 153–175.
- Pinheiro, D., Hannezo, E., Herszterg, S., Bosveld, F., Gaugue, I., Balakireva, M., Wang, Z., Cristo, I., Rigaud, S. U., Markova, O., et al.** (2017). Transmission of cytokinesis forces via E-cadherin dilution and actomyosin flows. *Nature* **545**, 103–107.
- Pitrone, P. G., Schindelin, J., Stuyvenberg, L., Preibisch, S., Weber, M., Eliceiri, K. W., Huysken, J. and Tomancak, P.** (2013). OpenSPIM: an open-access light-sheet microscopy platform. *Nat Methods* **10**, 598–599.
- Prat-Rojo, C., Pouille, P.-A., Buceta, J. and Martin-Blanco, E.** (2020). Mechanical coordination is sufficient to promote tissue replacement during metamorphosis in *Drosophila*. *EMBO J* **39**, e103594.
- Preibisch, S., Saalfeld, S. and Tomancak, P.** (2009). Globally optimal stitching of tiled 3D microscopic image acquisitions. *Bioinformatics* **25**, 1463–1465.
- Raffel, M., Willert, C. E., Scarano, F., Kähler, C., Wereley, S. T. and Kompenhans, J.** (2018). *Particle Image Velocimetry: A Practical Guide*. 3rd ed. Springer International Publishing.
- Ray, R. P., Matamoro-Vidal, A., Ribeiro, P. S., Tapon, N., Houle, D., Salazar-Ciudad, I. and Thompson, B. J.** (2015). Patterned Anchorage to the Apical Extracellular Matrix Defines Tissue Shape in the Developing Appendages of *Drosophila*. *Developmental Cell* **34**, 310–322.

- Rohrbach, A.** (2009). Artifacts resulting from imaging in scattering media: a theoretical prediction. *Opt Lett* **34**, 3041–3043.
- Sarov, M., Barz, C., Jambor, H., Hein, M. Y., Schmied, C., Suchold, D., Stender, B., Janosch, S., K J, V. V., Krishnan, R. T., et al.** (2016). A genome-wide resource for the analysis of protein localisation in *Drosophila*. *Elife* **5**, e12068.
- Schindelin, J., Arganda-Carreras, I., Frise, E., Kaynig, V., Longair, M., Pietzsch, T., Preibisch, S., Rueden, C., Saalfeld, S., Schmid, B., et al.** (2012). Fiji: an open-source platform for biological-image analysis. *Nat Methods* **9**, 676–682.
- Schmid, B., Shah, G., Scherf, N., Weber, M., Thierbach, K., Campos, C. P., Roeder, I., Aanstad, P. and Huiskens, J.** (2013). High-speed panoramic light-sheet microscopy reveals global endodermal cell dynamics. *Nat Commun* **4**, 2207.
- Siedentopf, H. and Zsigmondy, R.** (1902). Über Sichtbarmachung und Größenbestimmung ultramikroskopischer Teilchen, mit besonderer Anwendung auf Goldrubingläser. *Annalen der Physik* **315**, 1–39.
- Spletter, M. L., Barz, C., Yeroslaviz, A., Zhang, X., Lemke, S. B., Bonnard, A., Brunner, E., Cardone, G., Basler, K., Habermann, B. H., et al.** (2018). A transcriptomics resource reveals a transcriptional transition during ordered sarcomere morphogenesis in flight muscle. *eLife* **7**, e34058.
- Staier, F., Eipel, H., Matula, P., Evsikov, A. V., Kozubek, M., Cremer, C. and Hausmann, M.** (2011). Micro axial tomography: A miniaturized, versatile stage device to overcome resolution anisotropy in fluorescence light microscopy. *Review of Scientific Instruments* **82**, 093701.
- Strnad, P., Gunther, S., Reichmann, J., Krzic, U., Balazs, B., de Medeiros, G., Norlin, N., Hiiragi, T., Hufnagel, L. and Ellenberg, J.** (2016). Inverted light-sheet microscope for imaging mouse pre-implantation development. *Nat Methods* **13**, 139–142.
- Thévenaz, P., Ruttimann, U. E. and Unser, M.** (1998). A pyramid approach to subpixel registration based on intensity. *IEEE Trans Image Process* **7**, 27–41.
- Tomer, R., Khairy, K., Amat, F. and Keller, P. J.** (2012). Quantitative high-speed imaging of entire developing embryos with simultaneous multiview light-sheet microscopy. *Nature Methods* **9**, 755–763.
- Tuchin, V.** (2007). *Tissue Optics*. 1000 20th Street, Bellingham, WA 98227-0010 USA: SPIE.
- van Drongelen, R., Vazquez-Faci, T., Huijben, T. A. P. M., van der Zee, M. and Idema, T.** (2018). Mechanics of epithelial tissue formation. *Journal of Theoretical Biology* **454**, 182–189.
- Villedieu, A., Bosveld, F. and Bellaïche, Y.** (2020). Mechanical induction and competence in epithelial morphogenesis. *Curr Opin Genet Dev* **63**, 36–44.
- Voie, A. H., Burns, D. H. and Spelman, F. A.** (1993). Orthogonal-plane fluorescence optical sectioning: Three-dimensional imaging of macroscopic biological specimens. *Journal of Microscopy* **170**, 229–236.
- Wan, Y., McDole, K. and Keller, P. J.** (2019). Light-Sheet Microscopy and Its Potential for Understanding Developmental Processes. *Annu Rev Cell Dev Biol* **35**, 655–681.
- Wang, E., Babbey, C. M. and Dunn, K. W.** (2005). Performance comparison between the high-speed Yokogawa spinning disc confocal system and single-point scanning confocal systems. *Journal of Microscopy* **218**, 148–159.

Wayne S. Rasband (1997). *ImageJ*. U. S. National Institutes of Health, Bethesda, Maryland, USA.

Wu, Y., Wawrzusin, P., Senseney, J., Fischer, R. S., Christensen, R., Santella, A., York, A. G., Winter, P. W., Waterman, C. M., Bao, Z., et al. (2013). Spatially isotropic four-dimensional imaging with dual-view plane illumination microscopy. *Nature Biotechnology* **31**, 1032–1038.

Zitserman, D. and Roegiers, F. (2011). Live-cell Imaging of Sensory Organ Precursor Cells in Intact *Drosophila* Pupae. *JoVE (Journal of Visualized Experiments)* e2706.

Figures

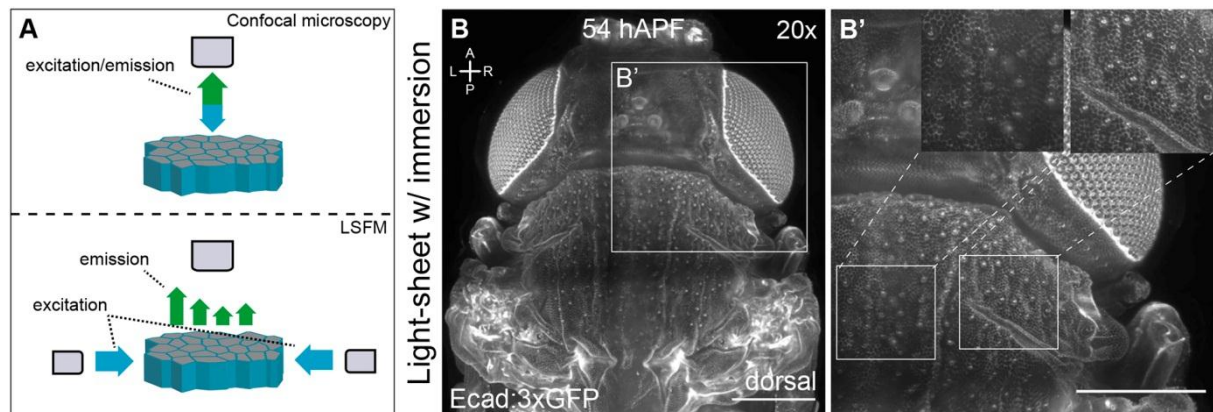


Figure 1 | Light-sheet microscopy imaging of an immersed *Drosophila* pupa.

A) Schematic of the difference in illumination/emission paths between dual-side illumination LSFM and confocal microscopy. In LSFM the illumination objective and the capturing objective are positioned at a 90° angle, while in confocal microscopy the same objective is used.

B) Dorsal view of a 54 hAPF Ecad:3xGFP expressing pupa imaged immersed in PBS using the Zeiss Z1 light-sheet microscope at 20x using dual-side illumination. The Anterior-Posterior (A-P) and Left-Right (L-R) axes are indicated. This image was acquired by tiling 2 x 2 images. $n=3$.

B') Close-up of the region outlined in (B) as well as close-up in the white square regions. See also Fig. S1 for fusion and deconvolution of the multi-angle light-sheet imaging of this sample.

The acquisition parameters are detailed in Table S1. Scale bars: 200 μm . n : number of animals.

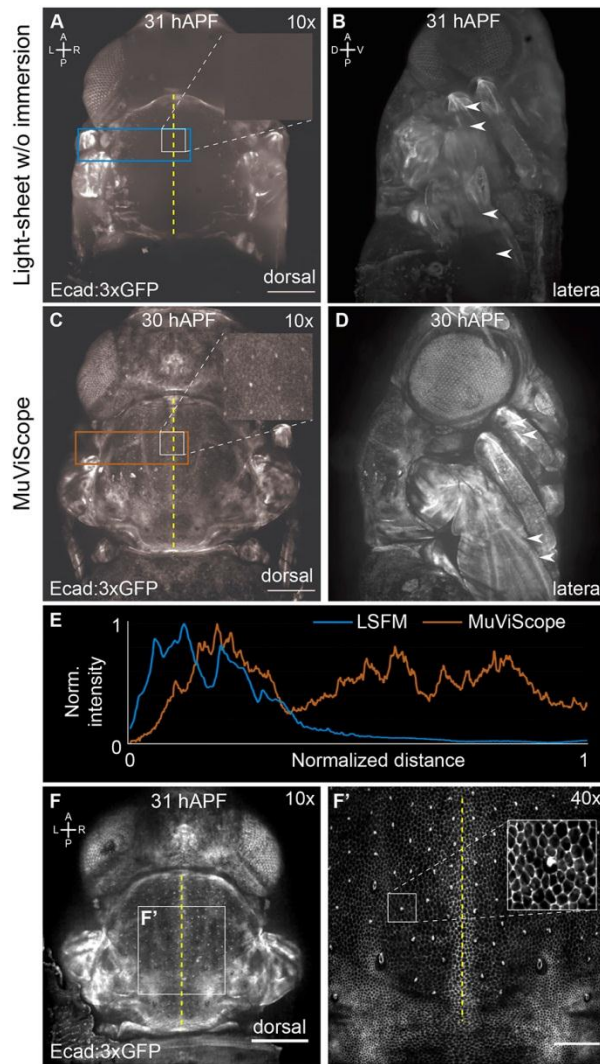


Figure 2 | Comparison of light-sheet microscopy to MuViScope.

A-P and L-R axes in A are indicated for A, C and the A-P and Dorsal-Ventral (D-V) axes in B for B, D. Insert positions are indicated by white rectangle. The midline is indicated by a yellow dashed line (A, C, F).

A) Dorsal view of a 31 hAPF Ecad:3xGFP expressing pupa without (w/o) immersion imaged using the Phaseview ALPHA3 microscope at 10x adapted for non-immersed dual-side illumination light-sheet microscopy. Close-up in the square region (insert) where image quality is lowest. $n=2$.

B) Lateral view of the pupa shown in A. Arrowheads indicate regions of large intensity differences in the leg and wing that are due to shadowing effects (compare D).

C) Dorsal view of a 30 hAPF Ecad:3xGFP expressing pupa imaged using the MuViScope at 10x. Close-up in the square region (inset) to illustrate the image quality obtained in the medial region of the pupa. $n=5$.

D) Lateral view of the pupa shown in C. Arrowheads indicate regions approximatively corresponding to the ones indicated in B to illustrate the more homogeneous signal intensities observed in the leg and wing when pupae are imaged using the MuViScope.

E) Graph of the normalized Ecad:3xGFP signal intensities within the rectangular regions shown in A (blue) and C (brown). Note that the normalized signal intensity in the sample imaged using LSFM (blue) goes to almost 0, while the MuViScope signal (brown) remains elevated throughout the sample.

F) Dorsal view of a 30 hAPF Ecad:3xGFP expressing pupa imaged with 10x and 40x objectives. The 10x view shows the overall animal shape. The white square region is imaged at higher resolution using the 40x objective and shown in F'. Cell outlines can be clearly ascertained in the inset in F'. $n=5$.

These images were acquired using a single xy position at 0 and 90° angles. The acquisition parameters are detailed in Table S1.

Scale bars: 200 μm (A-F), 50 μm (F'). n : number of animals.

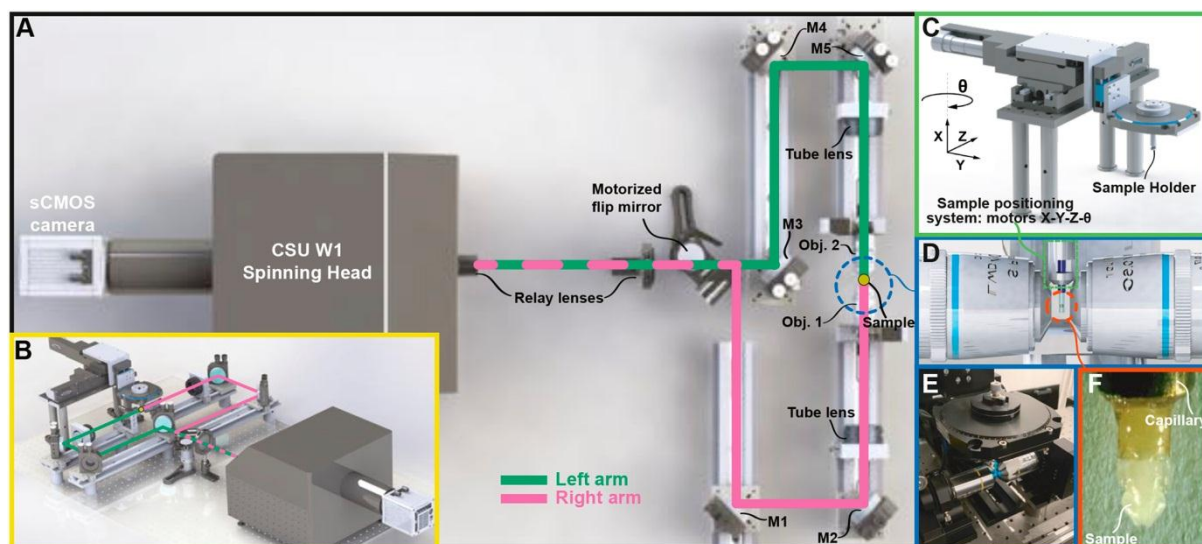


Figure 3 | Multi-View confocal microScope setup (MuViScope).

A) 3D rendering of the MuViScope setup. The MuViScope has two optical arms that illuminate the specimen and collect the fluorescence sequentially from the opposite side of the specimen: the optical pathway in pink for the right arm and the one in green for the left arm. Light is guided to the specimen through relay lenses, deflecting mirrors (M1-M5), tube lenses and objectives. The optical path is selected by a motorized flipping mirror.

B) Perspective view of the microscope with the two-colored optical pathways.

C) The capillary or the rod with the specimen is mounted in a custom-made sample holder. The specimen can be precisely positioned with three linear motors and one rotation motor to produce images from multiple views.

D) The two opposing dry objective lenses are focused onto two different planes to image two opposite views of the specimen.

E) Photo of the sample position system showing the sample holder and two objectives.

F) The sample is maintained at the end of a capillary.

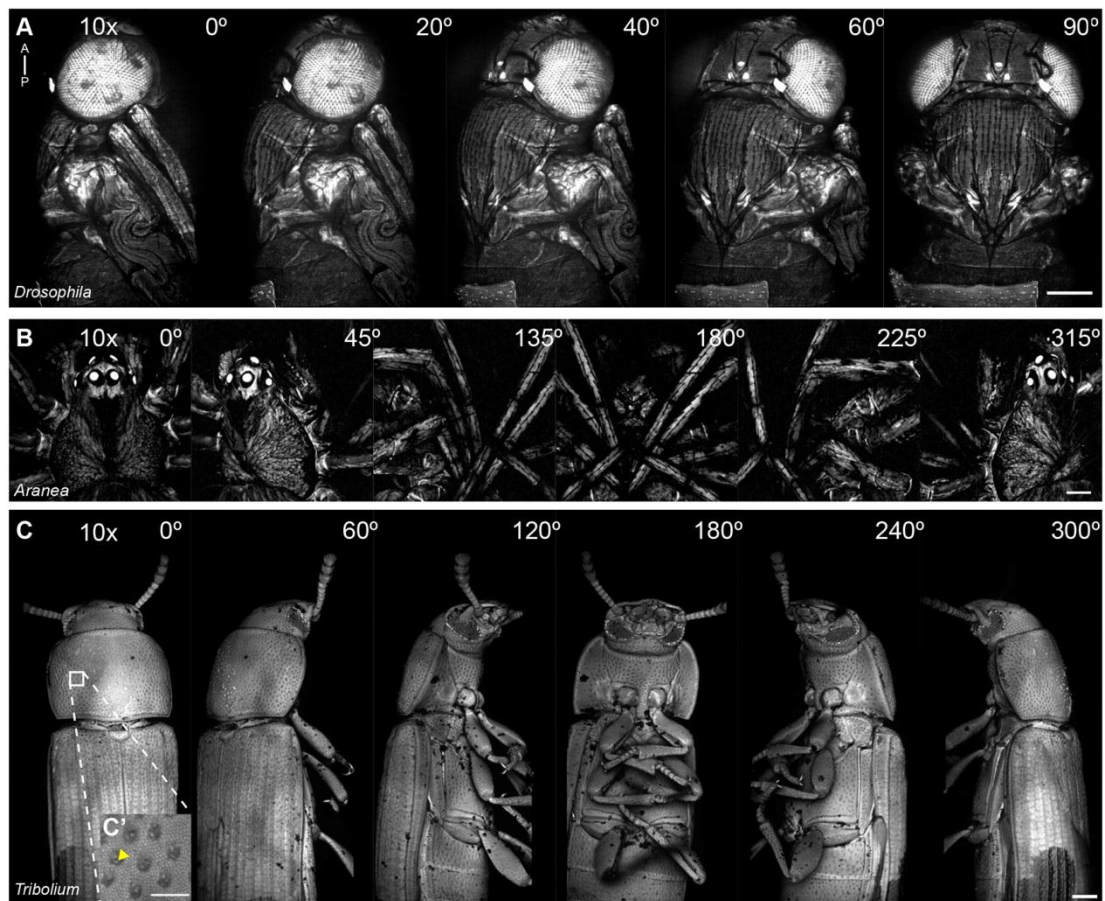


Figure 4 | Application of MuViScopy to multiple model organisms.

The A-P axis is indicated in A. Image collection is performed at 10x in A-C.

A) 5-angle 90° view of an Ecad:3xGFP pharate adult *Drosophila* without xy tilling. $n=2$.

B) 6-angle 315° view of a wild *Aranea* without xy tilling. Autofluorescence is used to image this sample. $n=1$.

C) 6-angle 300° view of an α tub1-LifeAct:GFP, EF1 α -nls:GFP adult *Tribolium* with 3 xy tilling positions along the A-P axis. See also Movie 2. $n=3$.

C') Close-up of the white box region in C. Yellow arrowhead: dimple in the outer chitin layer.

The acquisition parameters are detailed in Table S1. Scale bars: A-C 200 μ m, C' 50 μ m. n : number of animals.

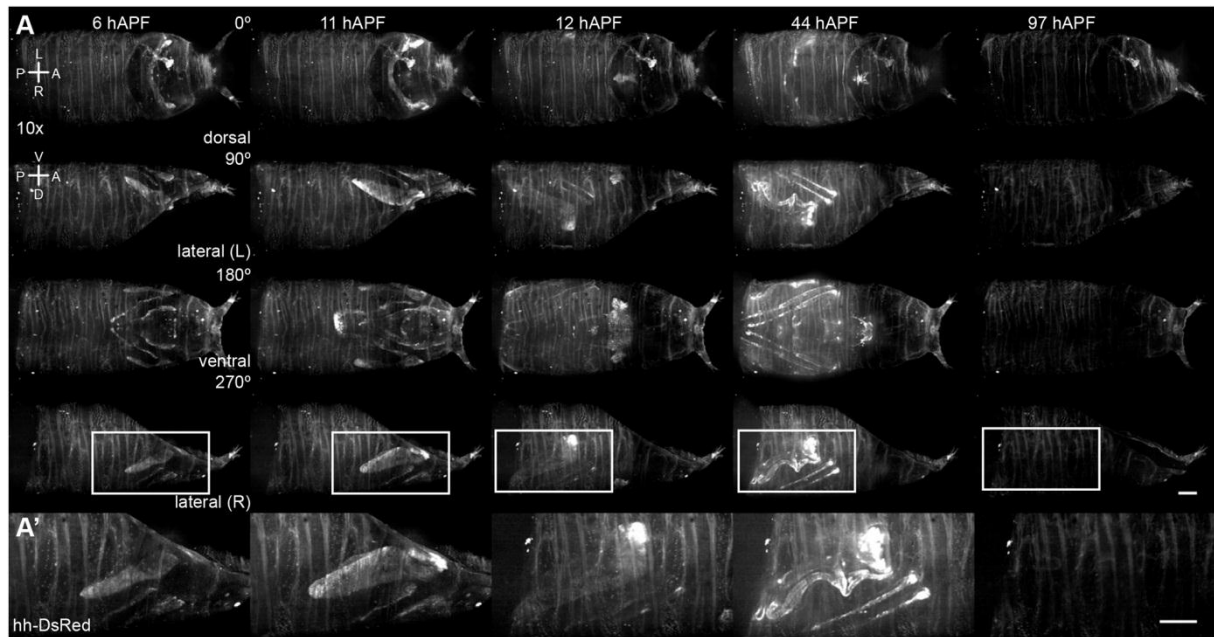


Figure 5 | Imaging through the *Drosophila* pupal case using hh-DsRed throughout pupal development.

A) 4-angle 360° view of a hh-DsRed pupa corresponding to dorsal, lateral right, ventral and lateral left views imaged at different time-points during pupal development. The wing posterior compartment undergoes a fast and global posterior movement at 11 ± 0.3 hAPF and started to undergo extensive twisting at 38 ± 0.7 hAPF ($n=3$). At time-point 97 hAPF the puparium is empty as the pupa has eclosed. The A-P and L-R axes are indicated on the dorsal view while the A-P and A-V are indicated on the lateral view. Image collection is performed at 10x with a two xy tiling along the A-P axis. See also Movie 3.

A') Close-up of the lateral (R) view indicated by white boxes in A.

The acquisition parameters are detailed in Table S1. Scale bars: 200 μ m. n : number of animals.

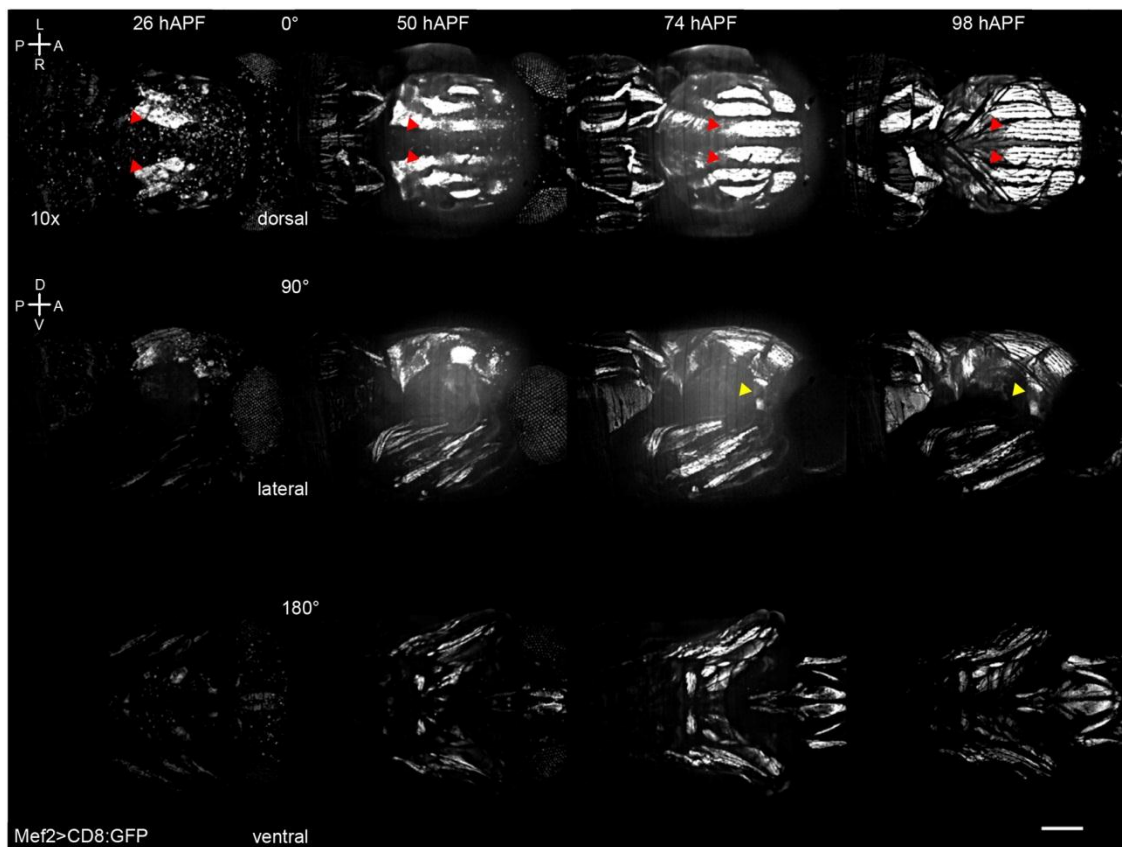


Figure 6 | Imaging of internal organs using the MuViScope.

The A-P and L-R axes are indicated on the dorsal view while the A-P and D-V axes are indicated on the lateral view. 3-angle view of a Mef2>CD8:GFP pupa corresponding to dorsal, lateral and ventral views imaged without tiling and a time step of 4 h during pupal development. Image collection was performed at 10x. Dorsal-longitudinal muscles: red arrowheads; dorsal-ventral muscles: yellow arrowheads. See also Movie 4. Similar results were obtained with a time-step of 12 h ($n=2$).

The complete acquisition parameters are detailed in Table S1. Scale bar: 200 μm . n : number of animals.

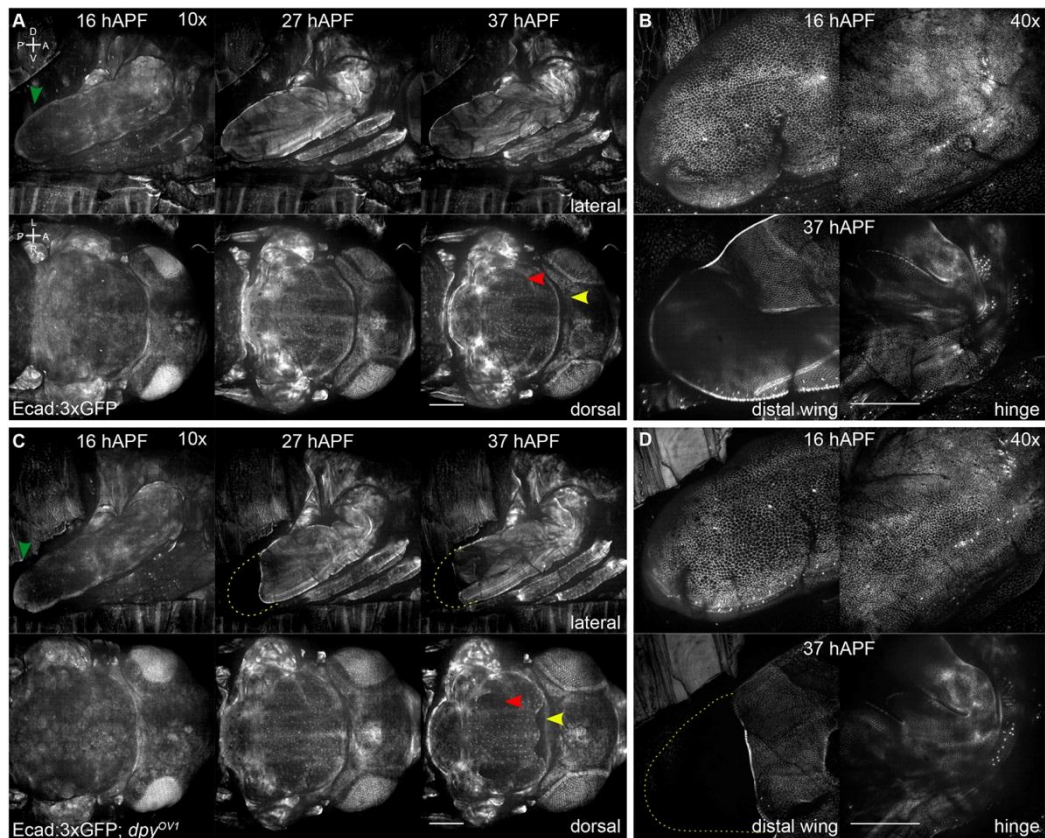


Figure 7 | Imaging of multiple organs in wt and *dpy*^{OV1} *Drosophila* pupae.

Green arrowheads: time-point when distal wing is similarly shaped in both conditions. Yellow arrowheads: position of the anterior comma like invaginations in Ecad:3xGFP, *dpy*^{OV1}. The arrowhead points to a similar position in Ecad:3xGFP, wt for comparison. Red arrowheads: position of a lateral pit in Ecad:3xGFP, *dpy*^{OV1}. The arrowhead points to a similar position in Ecad:3xGFP, wt for comparison.

A) 2-angle 90° views of Ecad:3xGFP pupa corresponding to the lateral and dorsal views at 16, 27 and 37 hAPF using a 10x objective on the first MuViScope arm. The A-P and D-V axes are indicated on the lateral view while the A-P and L-R axes are indicated on the dorsal view. The hinge contraction was set to begin at 17 hAPF and is associated with distal to proximal tissue flow in the wing blade (Aigouy et al., 2010; Etournay et al., 2015; Guirao et al., 2015). The anterior to posterior tissue flow in the notum occurs at 21.5 ± 0.9 hAPF ($n=3$).

B) Lateral view of the pupa shown in A using the 40x objective on the second microscope optical arm at two distinct not-tiled positions along the A-P axis to image both the wing most distal part (left) and the hinge (right).

C) 2-angle 90° views of Ecad:3xGFP, *dpy^{OV1}* pupa corresponding to the lateral and dorsal views at 16, 27 and 37 hAPF using a 10x objective on the first MuViScope arm. The hinge contraction was set to begin at 17 hAPF. The anterior posterior tissue flow in the *dpy^{OV1}* notum occurs at 21.1 ± 0.9 hAPF ($n=3$). Anterior comma-like invaginations and posterior lateral pits can be observed in the notum at 25.1 ± 2.8 and 26.5 ± 2.4 hAPF ($n=3$), respectively.

Dashed lines: delineates approximate shape of a wt wing.

D) Lateral view of the pupa shown in C using the 40x objective on the second microscope arm at two distinct not-tiled positions along the A-P axis to image both the wing most distal part (left) and the hinge (right). Dashed lines: delineates approximate shape of a wt wing.

The acquisition parameters are detailed in Table S1. Scale bars: A, C 100 μm and B, D 50 μm . See also Movie 5. n : number of animals.

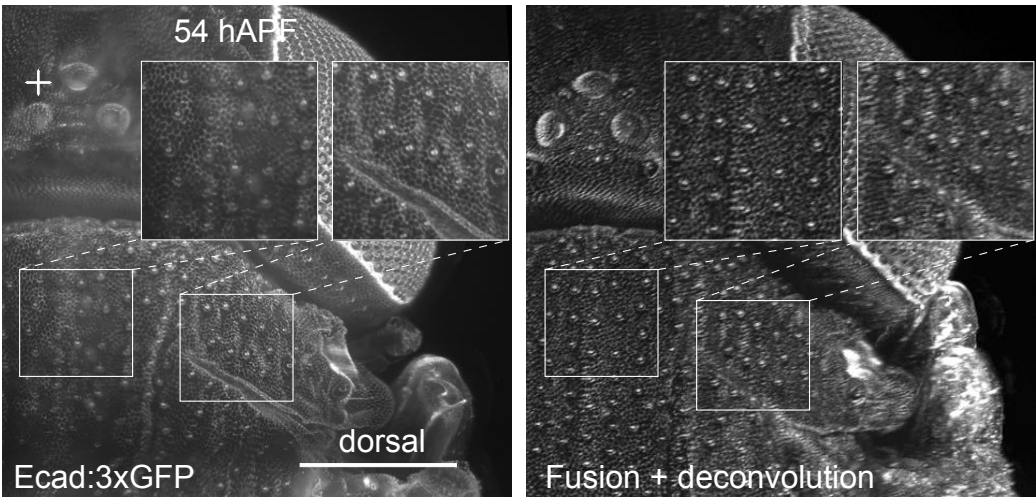


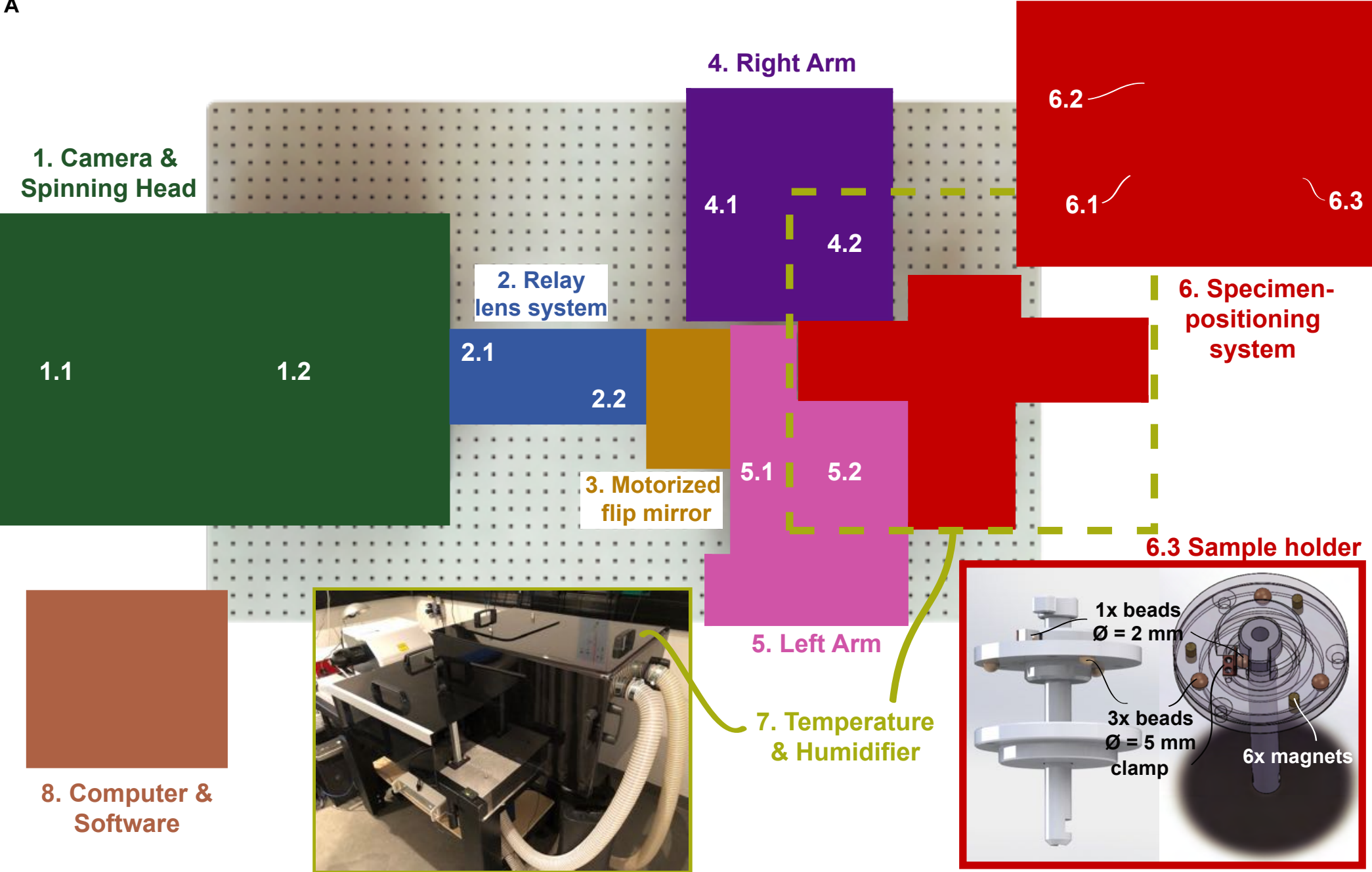
Fig. S1. Fusion and deconvolution of a multi-angle light-sheet microscopy imaging of an immersed *Drosophila* pupa.

Dorsal view of a 54 hAPF Ecad:3xGFP expressing pupa immersed in PBS imaged using the Zeiss Z1 light-sheet microscope at 20x using dual-side illumination. The Anterior-Posterior (A-P) and Left-Right (L-R) axes are indicated. Close-ups in the white square regions (insets) are shown to better visualize the cellular resolution. The same pupa is shown in Fig. 1B.

- A) Maximum projection of an image stack from one angle.
- B) Fusion and deconvolution of the same sample obtained under 4 angles (0/90/180/270°). The insets show an improved quality in the medial part of the notum over the non-fused/deconvolved image in A.

The acquisition parameters are detailed in Table S1. Scale bar: 200 μm

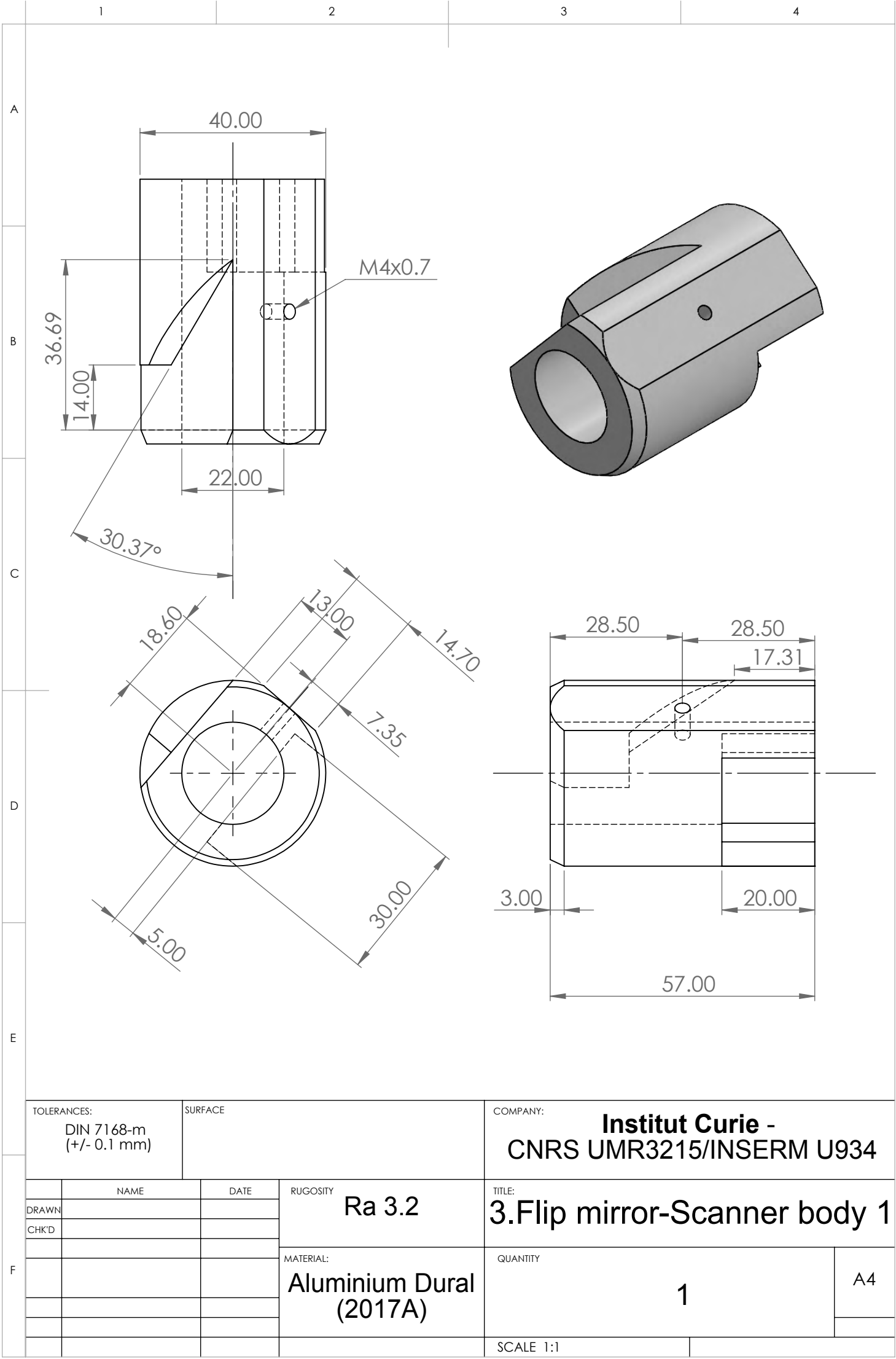
A

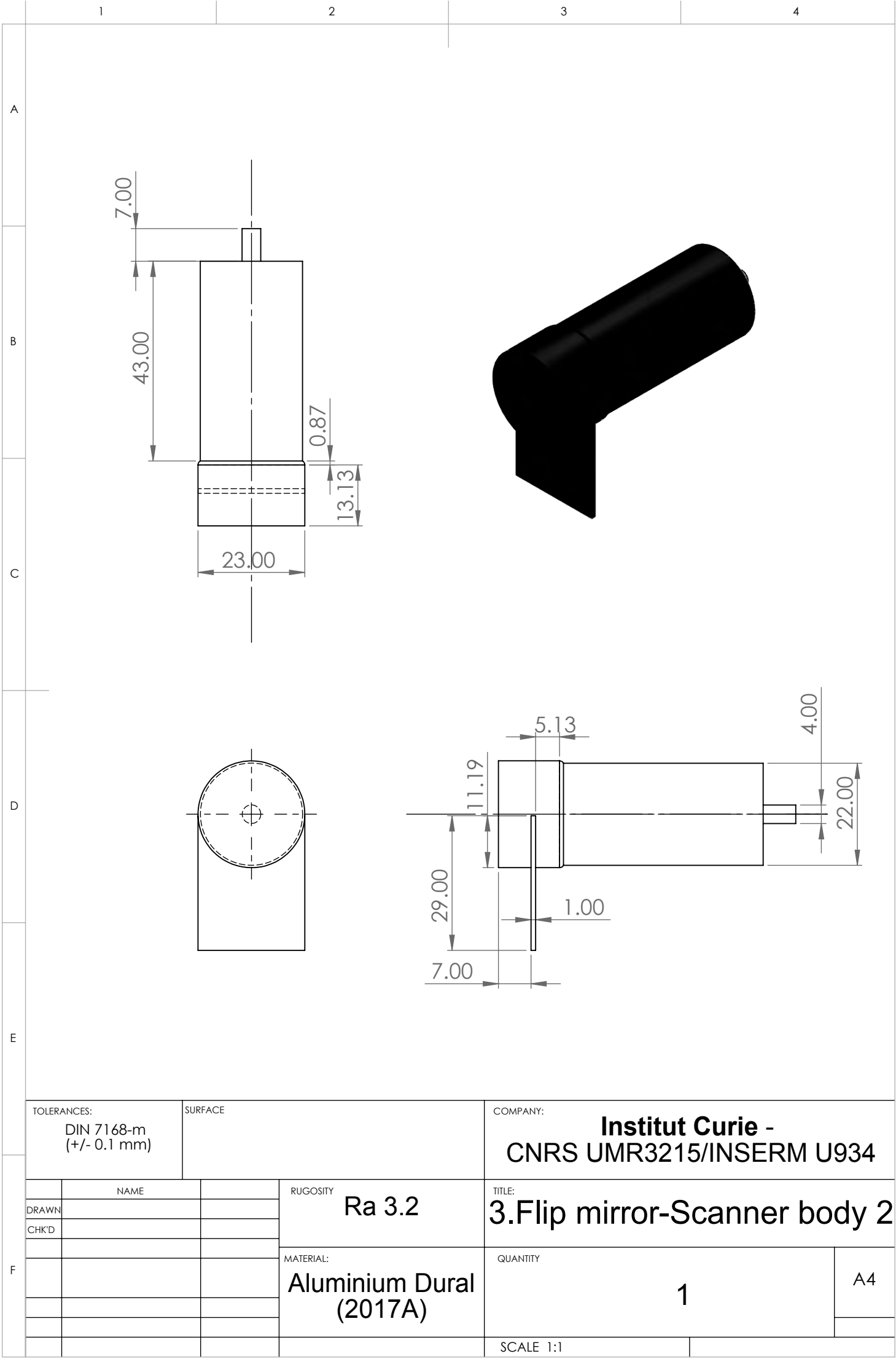


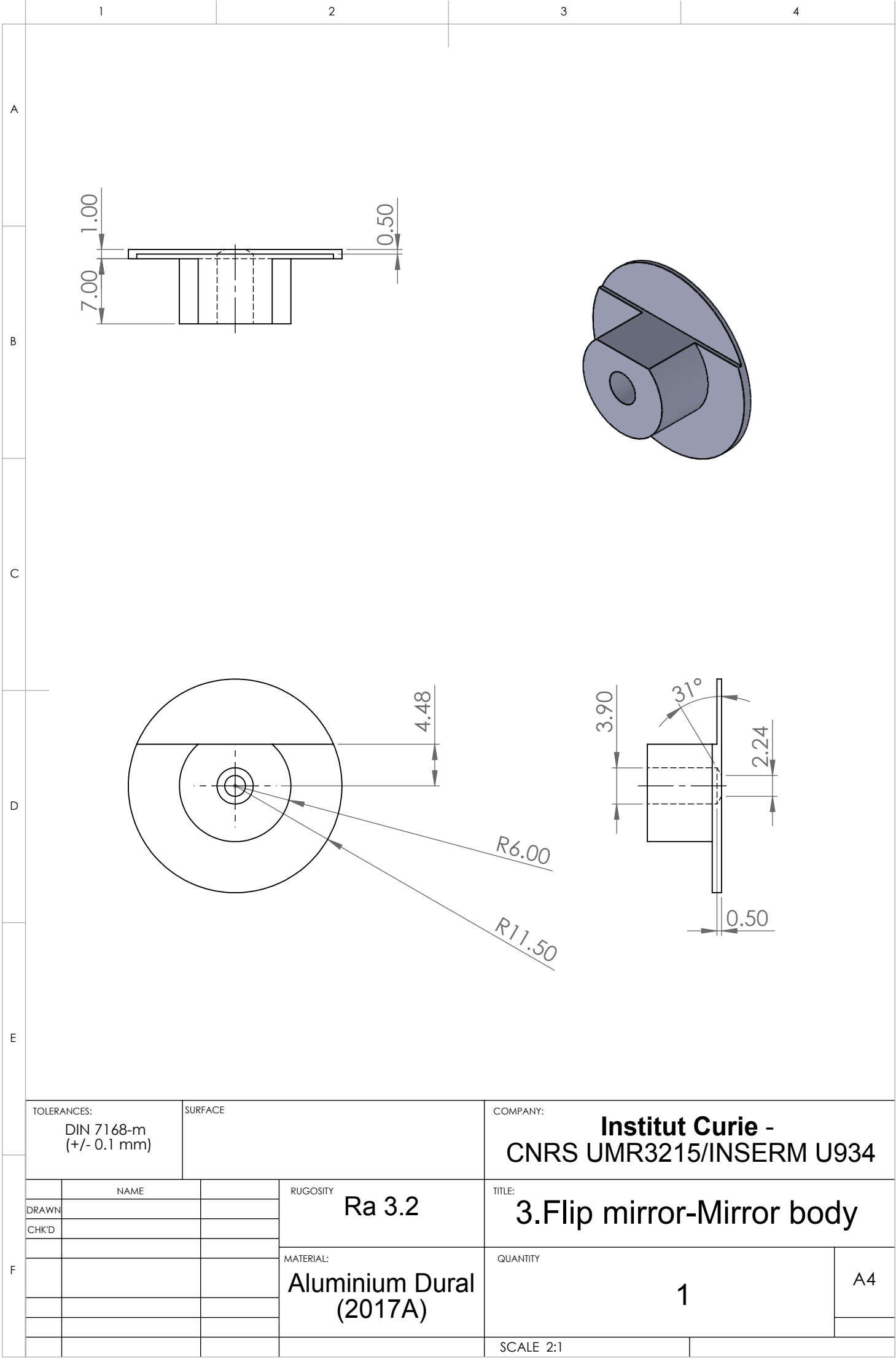
B

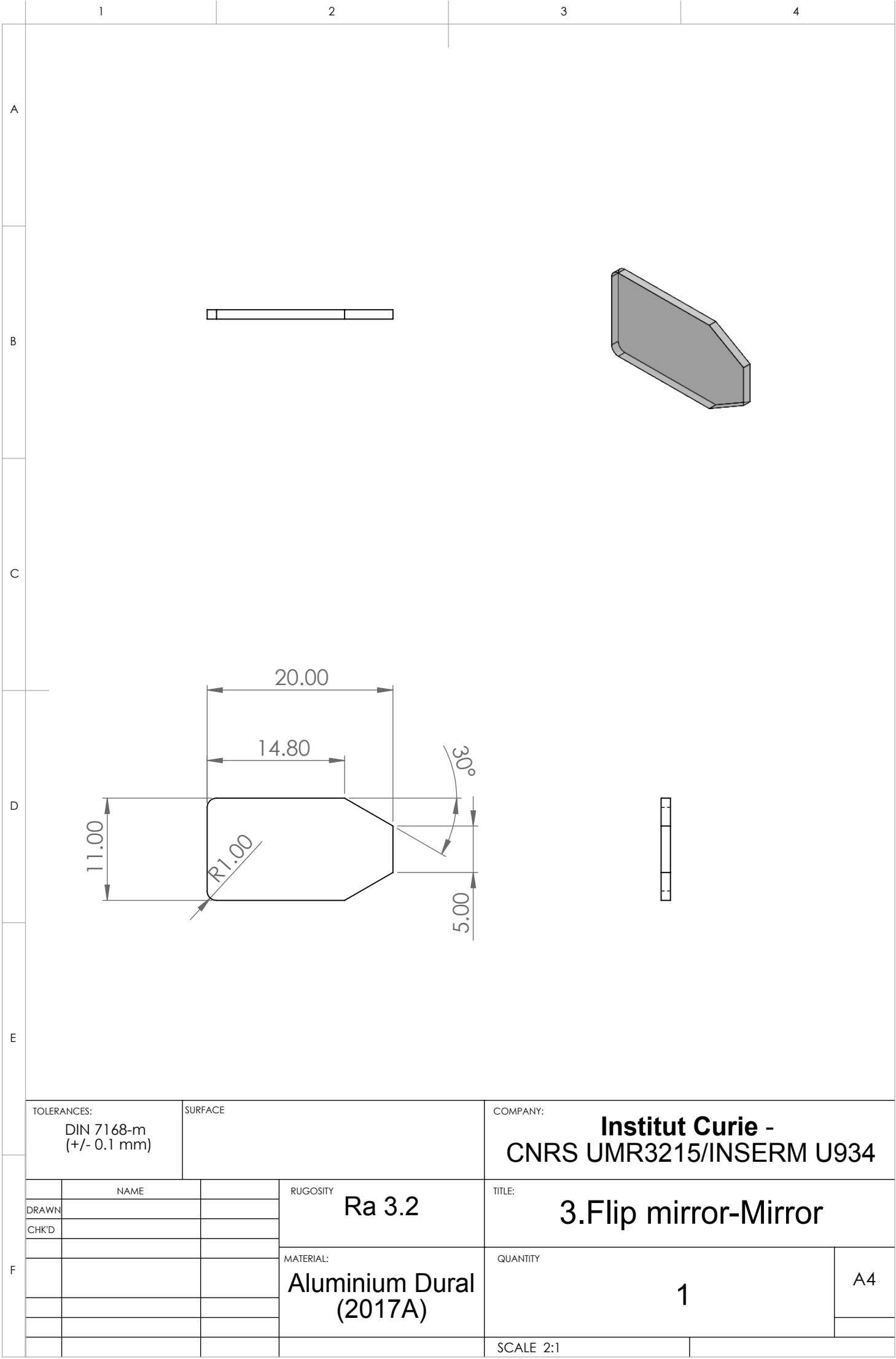
List of Materials of the MuViScope

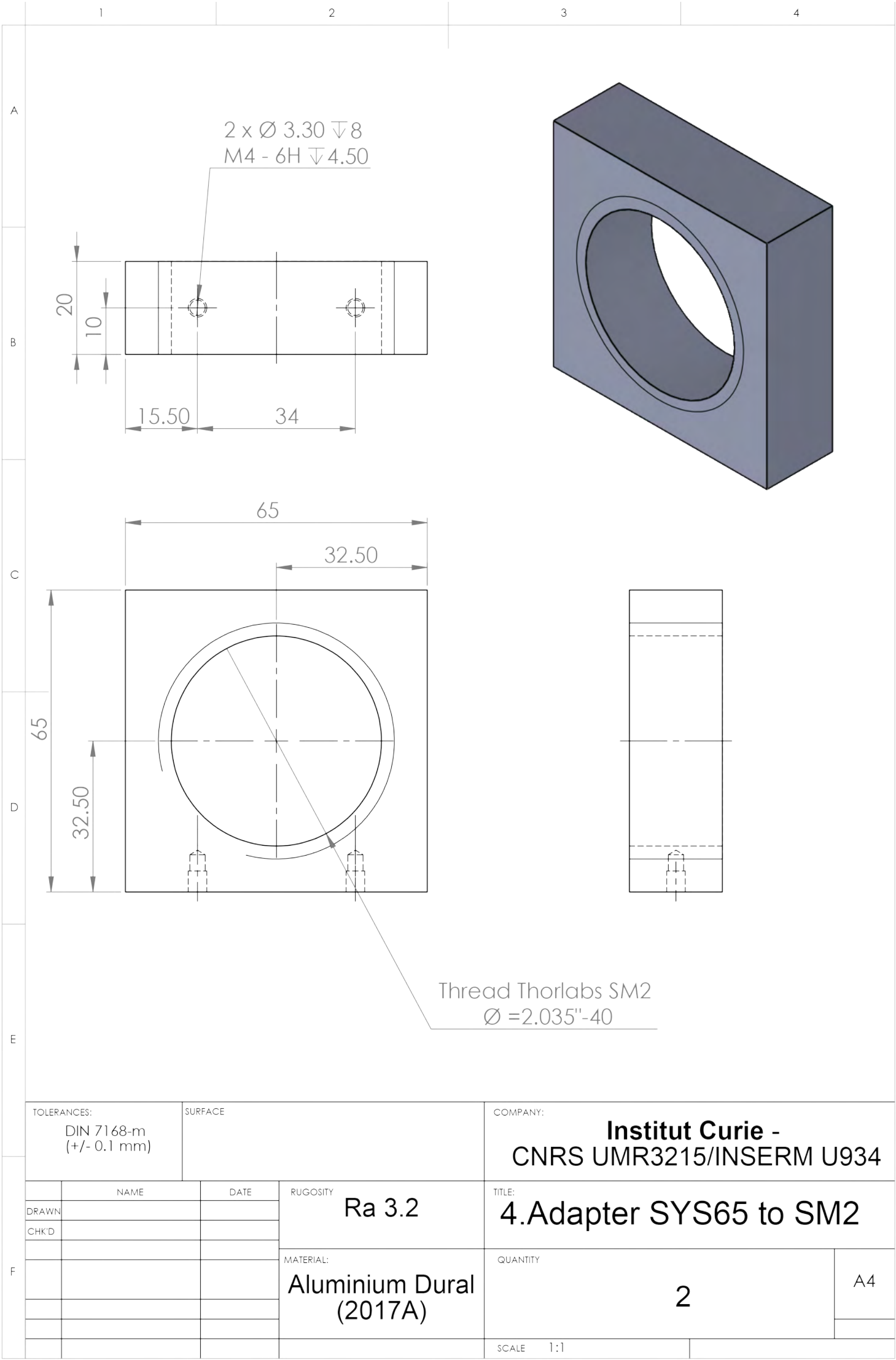
Position	Quantity	Description	Manufacturer	Part number
1. Camera & Spinning Head				
1.1	1	Camera ORCA-FLASH4.0 V2 + CAMERALINK PACK FLASH4	Hamamatsu	C1140-22C
1.2	1	Visiscope Yokogawa CSU-W1-T2 with variable aperture	Andor Technology	CSU-W1-T2
not shown	1	Laser combiner with 405 (150mW), 488 (150mW), 561 (100mW) , 645 nm (100mW) wavelength	GATACA systems	
2. Relay lens system				
2.1	1	SM1 Lens Tube, 1.00" Thread Depth	Thorlabs	SM1L10
2.1	1	Mirror f = 200 mm, Ø1" Achromatic Doublet, Unmount, AR Coated: 400 - 700 nm	Thorlabs	AC254-200-A
2.2	1	Mounting Base, 25 mm x 58 mm x 10 mm	Thorlabs	BA1S/M
2.2	1	Ø12.7 mm Post Holder, Spring-Loaded Hex-Locking Thumbscrew, L=40 mm	Thorlabs	PH40/M
2.2	1	Ø12.7 mm Optical Post, SS, M4 Setscrew, M6 Tap, L = 40 mm	Thorlabs	TR40/M
2.2	1	Slip Ring for SM2 Lens Tubes, M4 Tap	Thorlabs	SM2RC/M
2.2	1	Mirror f = 200 mm, Ø2" Achromatic Doublet, SM2-Threaded Mount, AR Coated: 400 - 700 nm	Thorlabs	AC508-200-A-ML
3. Motorized flip mirror				
3	1	Clamping Fork for Ø1.5" Pedestal Post or Post Pedestal Base Adapter, Universal	Thorlabs	PF175
3	1	Variable Height P-Post	Thorlabs	BLP01/M
3	1	Compact Ø1.5" Post Mounting Clamp, Included Quick-Release Handle, Metric	Thorlabs	C1510/M
3	1	Motorized flip mirror (Scanner body Part 1)	Errol Laser	Drawing: 3.Flip Mirror-Scanner Body 1
3	1	Motorized flip mirror (Scanner body Part 2)	Errol Laser	Drawing: 3.Flip Mirror-Scanner Body 2
3	1	Flip Mirror - Scanner Body 1	Errol Laser	Drawing: 3.Flip Mirror-Mirror Body
3	1	Custom-cut dielectric mirror 400-700 nm designed for use at a 45° angle of incidence	Errol Laser	Drawing: 3.Flip Mirror-Mirror
3	1	Home controller for flip mirror	Errol Laser	Custom-made
4. Right Arm				
4.1	2	Mounting Post Spacer, Height = 20 mm	Thorlabs	PS20M
4.1	2	Ø1.5" Mounting Post, M6 Taps, L = 25 mm	Thorlabs	P25/M
4.1	1	System rail 65, 300 mm long, with slotted holes	OWIS	16.011.0300
4.1	1	Ø25.4 mm Gimbal Mirror Mount, Metric, One Retaining Ring Included	Thorlabs	GM100/M
4.1	1	Slide RT 65, 65 mm, with hexagon socket head cap screw ISO 4762	OWIS	16.022.0065
4.1	1	Ø2" Broadband Dielectric Mirror, 400 - 750 nm	Thorlabs	BB2-E02
4.2	2	Mounting Post Spacer, Height = 20 mm	Thorlabs	PS20M
4.2	2	Ø1.5" Mounting Post, M6 Taps, L = 25 mm	Thorlabs	P25/M
4.2	1	System rail 65, 300 mm long, with slotted holes	OWIS	16.011.0300
4.2	1	Ø25.4 mm Gimbal Mirror Mount, Metric, One Retaining Ring Included	Thorlabs	GM100/M
4.2	1	Slide RT 65, 65 mm, with hexagon socket head cap screw ISO 4762	OWIS	16.022.0065
4.2	1	Ø2" Broadband Dielectric Mirror, 400 - 750 nm	Thorlabs	BB2-E02
4.2	1	Slide RT 65, 20 mm, with hexagon socket head cap screw ISO 4762	OWIS	16.022.0020
4.2	1	Adapter with External SM2 Threads and Internal M38 x 0.5 Threads	Thorlabs	SM2A20
4.2	1	Adapter from OWIS SYS65 to Thorlabs SM2	Custom-made	Drawing: 4.Adapter SYS65 to SM2
4.2	1	Tube Lens 1X (F=200MM), Thread M35x0.5, Optical diameter = 32mm	Nikon Instruments Inc	MXA20696
4.2	1	Raised slide SYS 65, 25 mm, with hexagon socket head cap screw ISO 4762	OWIS	16.022.2025
4.2	1	Adapter from Thorlabs SM1ZP to OWIS 16.022.2025	Custom-made	Drawing: 4.Adapter SYS65 to SM1ZP
4.2	1	Z-Axis Translation Mount, Post Mountable, M6 and M4 Taps	Thorlabs	SM1ZP/M
4.2	1	Microscope objective to SM1 Adapter	Thorlabs	SM1A3
4.2	1	CFI Plan Apo Lambda 10X /0.45 or CFI S Plan Fluor ELWD 40XC/0.6	Nikon Instruments Inc	MRD00105 or MRH08430
5. Left Arm				
5.1	2	Mounting Post Spacer, Height = 20 mm	Thorlabs	PS20M
5.1	2	Ø1.5" Mounting Post, M6 Taps, L = 25 mm	Thorlabs	P25/M
5.1	2	System rail 65, 300 mm long, with slotted holes	OWIS	16.011.0300
5.1	2	Ø25.4 mm Gimbal Mirror Mount, Metric, One Retaining Ring Included	Thorlabs	GM100/M
5.1	2	Slide RT 65, 65 mm, with hexagon socket head cap screw ISO 4762	OWIS	16.022.0065
5.1	2	Ø2" Broadband Dielectric Mirror, 400 - 750 nm	Thorlabs	BB2-E02
5.2	2	Mounting Post Spacer, Height = 20 mm	Thorlabs	PS20M
5.2	2	Ø1.5" Mounting Post, M6 Taps, L = 25 mm	Thorlabs	P25/M
5.2	1	System rail 65, 300 mm long, with slotted holes	OWIS	16.011.0300
5.2	1	Ø25.4 mm Gimbal Mirror Mount, Metric, One Retaining Ring Included	Thorlabs	GM100/M
5.2	1	Slide RT 65, 65 mm, with hexagon socket head cap screw ISO 4762	OWIS	16.022.0065
5.2	1	Ø2" Broadband Dielectric Mirror, 400 - 750 nm	Thorlabs	BB2-E02
5.2	1	Slide RT 65, 20 mm, with hexagon socket head cap screw ISO 4762	OWIS	16.022.0020
5.2	1	Adapter with External SM2 Threads and Internal M38 x 0.5 Threads	Thorlabs	SM2A20
5.2	1	Adapter from OWIS SYS65 to Thorlabs SM2	Custom-made	Drawing: 4.Adapter SYS65 to SM2
5.2	1	Tube Lens 1X (F=200MM), Thread M35x0.5, Optical diameter = 32mm	Nikon Instruments Inc	MXA20696
5.2	1	Raised slide SYS 65, 25 mm, with hexagon socket head cap screw ISO 4762	OWIS	16.022.2025
5.2	1	Adapter from Thorlabs SM1ZP to OWIS 16.022.2025	Custom-made	Drawing: 4.Adapter SYS65 to SM1ZP
5.2	1	Z-Axis Translation Mount, Post Mountable, M6 and M4 Taps	Thorlabs	SM1ZP/M
5.2	1	Microscope objective to SM1 Adapter	Thorlabs	SM1A3
5.2	1	CFI Plan Apo Lambda 10X /0.45 or CFI S Plan Fluor ELWD 40XC/0.6	Nikon Instruments Inc	MRD00105 or MRH08430
6. Specimen-positioning system				
6.1	4	Clamping Fork, 9.5 mm Counterbored Slot, M6 x 1.0 Captive Screw	Thorlabs	CF038CM
6.1	4	Ø31.8 mm Sludded Pedestal Base Adapter, M6 Thread	Thorlabs	BE1/M
6.1	4	Ø25.0 mm Pillar Post, M6 Taps, L = 150 mm	Thorlabs	RS150/M
6.1	1	100 mm x 600 mm x 12.7 mm Aluminum Breadboard, M6 Double-Density Taps	Thorlabs	MB1060/M
6.2	2	Precision linear stage, ballscrew, width 80 mm, 25 mm travel range, DC gear motor	Physik Instrumente	M-404.1DG
6.2	1	Translation Stage, 15 mm, DC Motor Gearhead	Physik Instrumente	M-111.1DG
6.2	1	PiLine Rotation Stage Fast Positioning, Ultra-Low Profile, Ø 108 mm, 360°, 34 µrad Resolution	Physik Instrumente	M-660-55
not shown	1	4 axes Motion Controller	Physik Instrumente	C-884.4DC
6.2	1	Adapter from M-404 to M-111 (Part 1)	Custom-made	Drawing: 6.Adapter M404 to M111-1
6.2	1	Adapter from M-404 to M-111 (Part 2)	Custom-made	Drawing: 6.Adapter M404 to M111-2
6.2	1	Adapter from M-111 to M-660 (Part 1)	Custom-made	Drawing: 6.Adapter M111 to M660-1
6.2	1	Adapter from M-111 to M-660 (Part 2)	Custom-made	Drawing: 6.Adapter M111 to M660-2
6.3	3	Stainless steel beads, Ø = 5 mm	123Roulement	BA-5-INOX-AISI420
6.3	1	Stainless steel beads, Ø = 2 mm	123Roulement	BA-2-INOX-316
6.3	6	Magnet-Cylinder Z03x03Ni-N52	HKCM Engineering	9962-67948
6.3	1	Adapter M660 to Sample Holder - Bottom part	Custom-made	Drawing: 6.Adapter M660 to Sample Holder - Bottom
6.3	1	Adapter M660 to Sample Holder - Top part	Custom-made	Drawing: 6.Adapter M660 to Sample Holder - Top
6.3	1	Sample Holder	Custom-made	Drawing: 6.Sample Holder
6.3	1	Sample Holder Clamp	Custom-made	Drawing: 6.Sample Holder Clamp
7. Temperature & Humidifier				
not shown	1	Humidifier EVA	Stadler Form	
not shown	1	Temperature Controller Cube	Life Imaging System	
7	1	Custom Thermostatic Chamber	Errol Laser	Custom-made
8. Computer & Software				
8	1	Dell T7610, 2CPU, 32Go, SSD RAID	Dell	
8	1	Metamorph software	Molecular Devices	

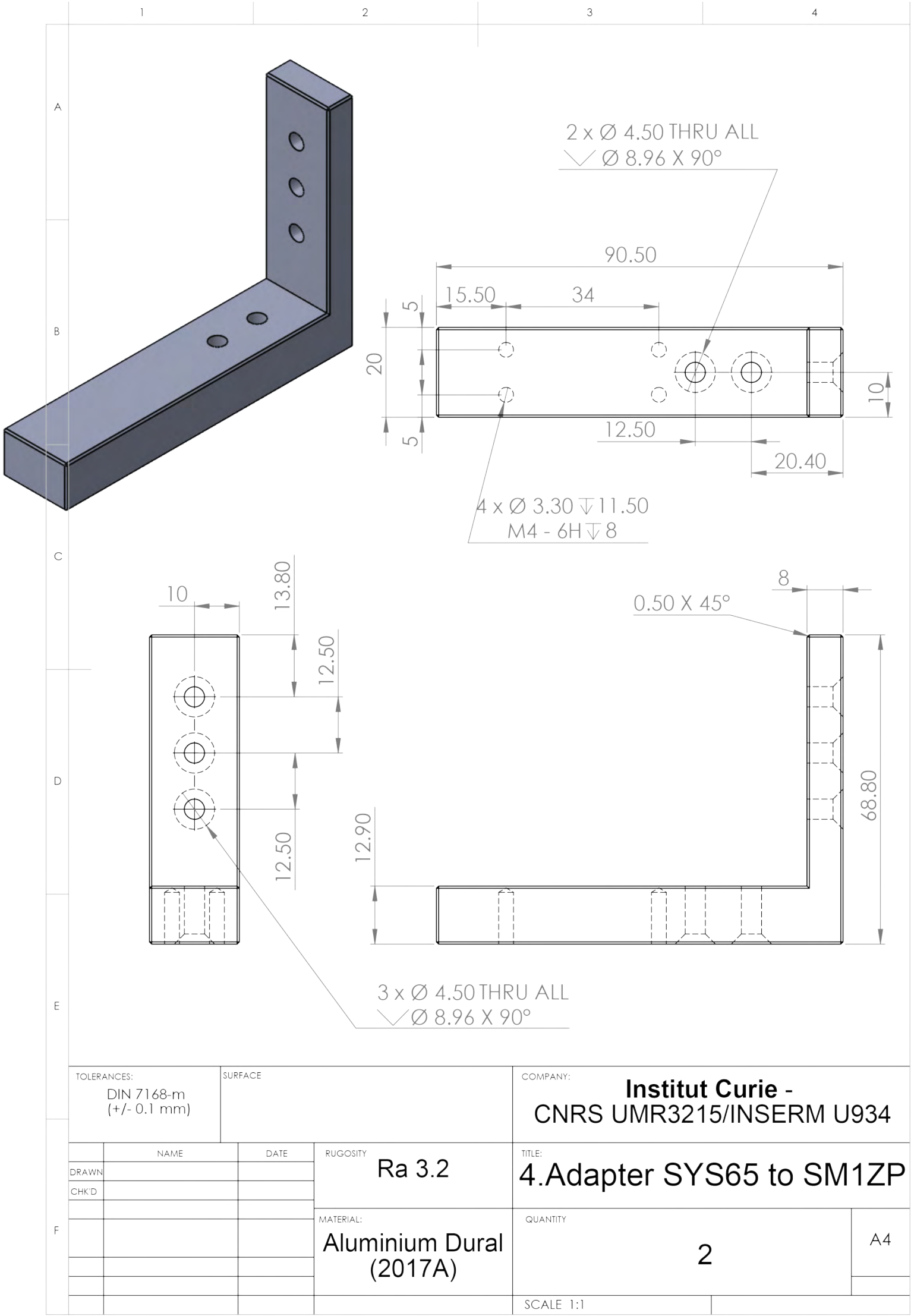


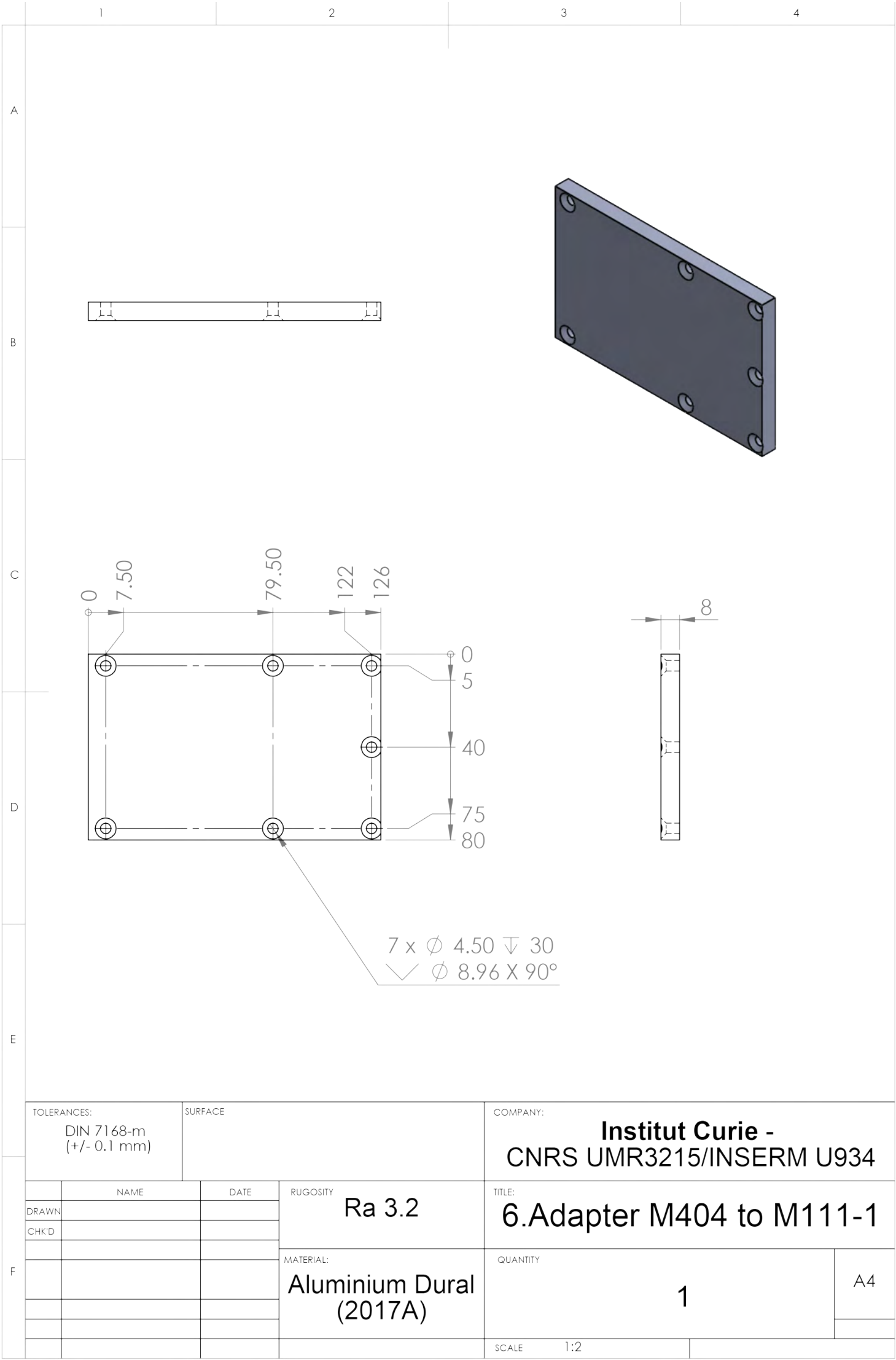


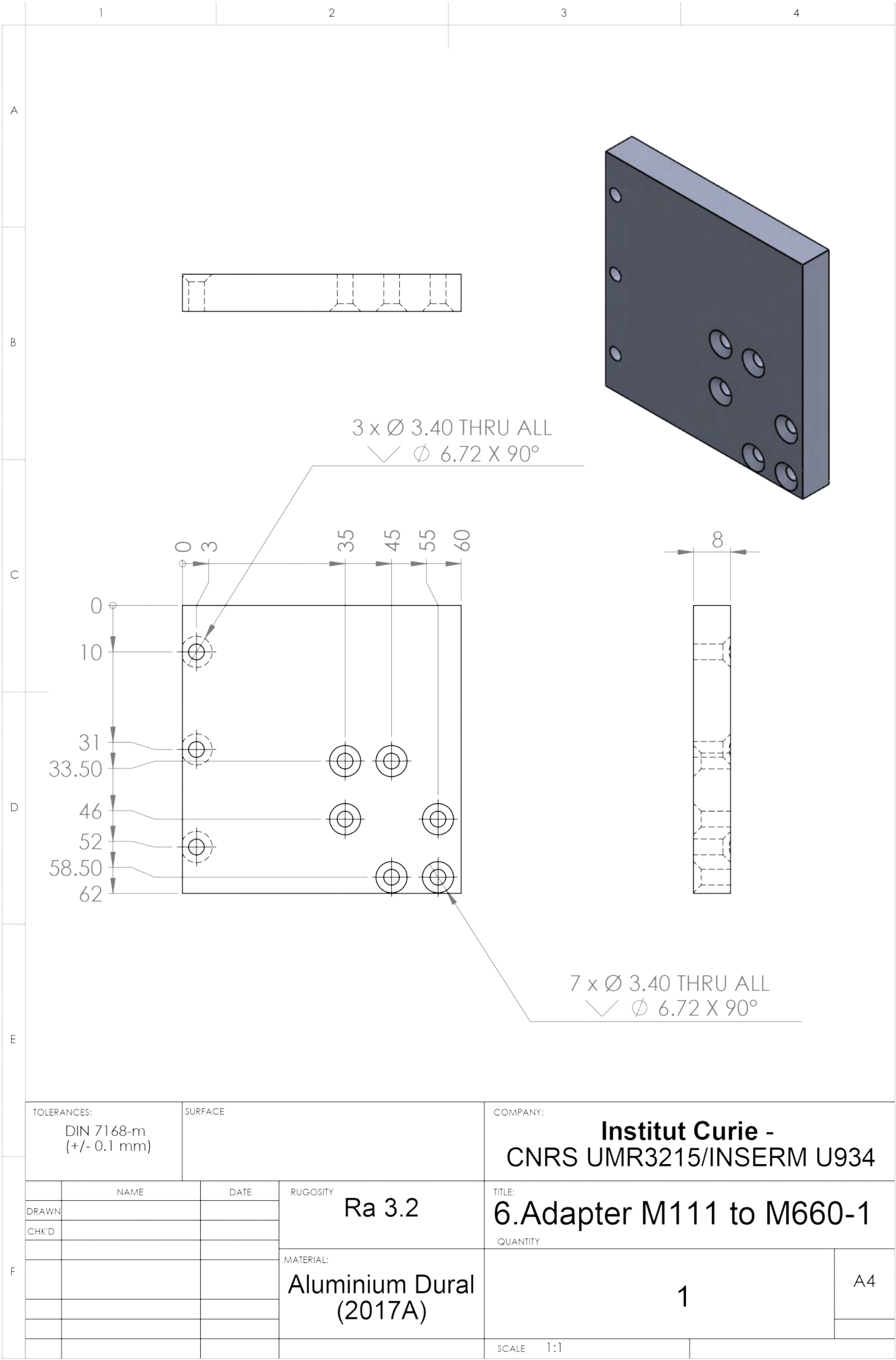












1

2

3

4

A

COUPE B-B

3 x hemisphere hole for bead Ø 5

B

C

3 x Ø 3.5

3 x Ø 3.40THRU ALL
✓ Ø 6.72 X 90°

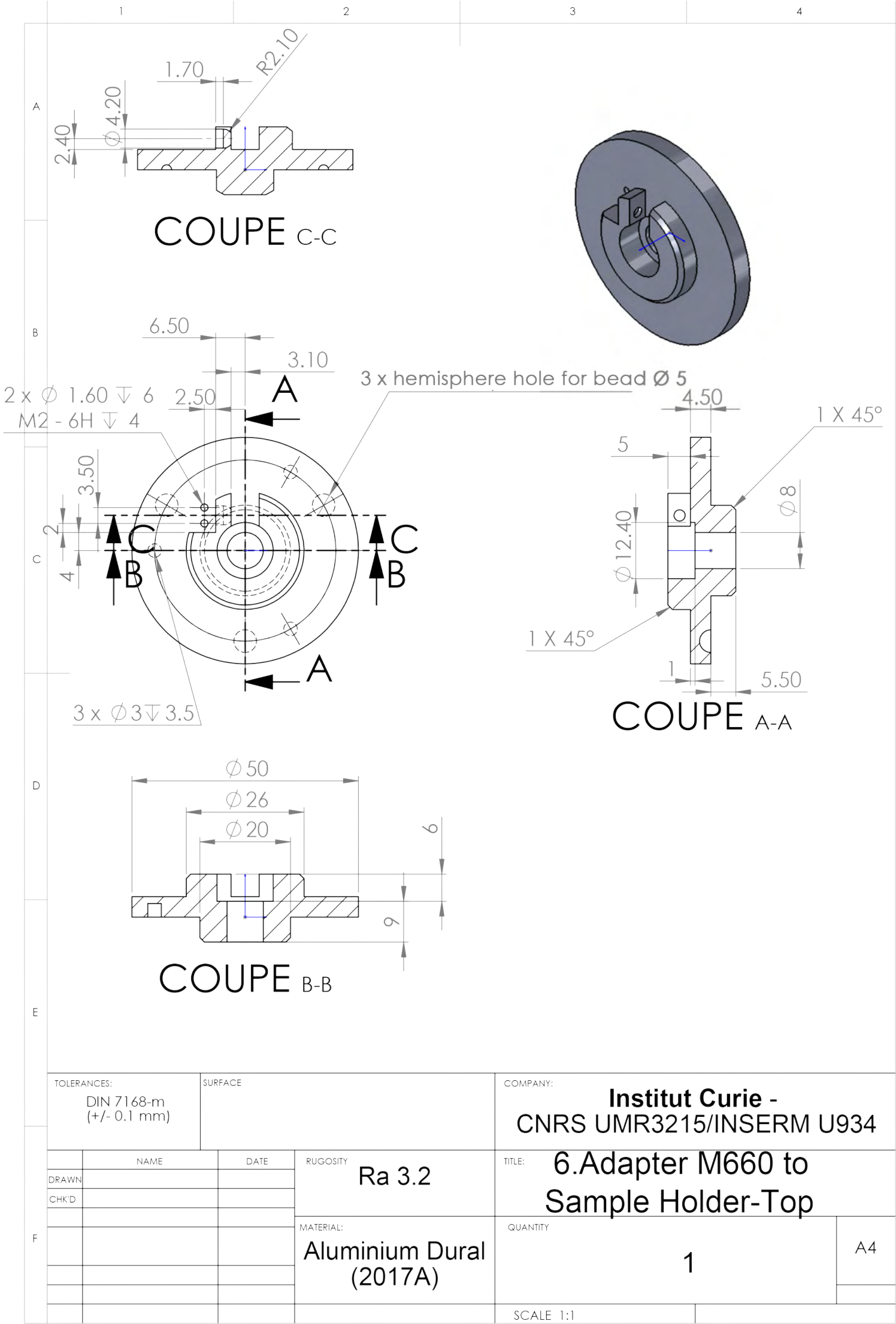
D

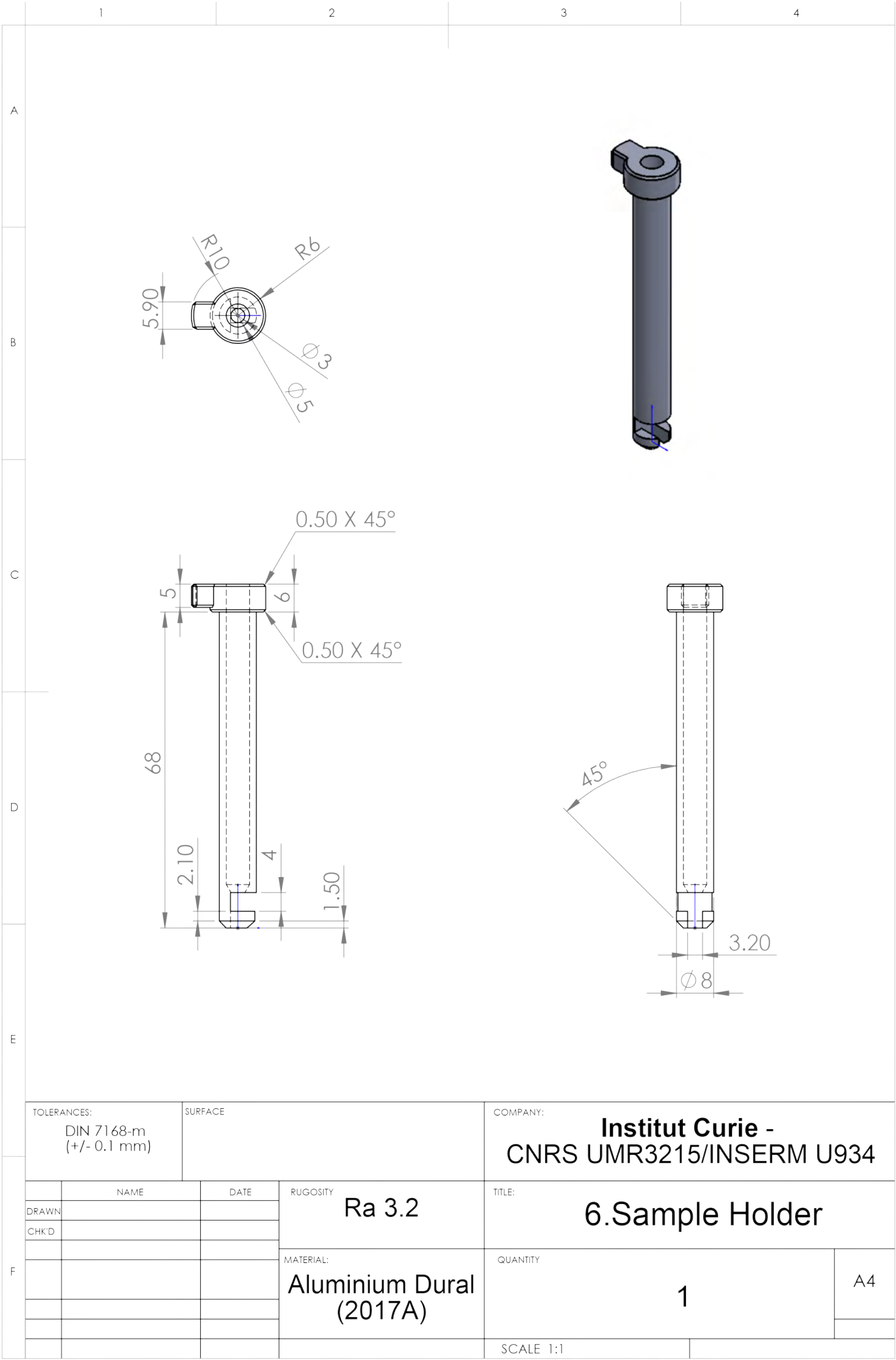
COUPE A-A

E

TOLERANCES: DIN 7168-m (+/- 0.1 mm)			SURFACE		COMPANY: Institut Curie - CNRS UMR3215/INSERM U934		
	NAME	DATE	RUGOSITY Ra 3.2		TITLE: 6.Adapter M660 to Sample Holder-Bottom		
DRAWN							
CHK'D			MATERIAL: Aluminium Dural (2017A)		QUANTITY 1		A4
					SCALE 1:1		

F





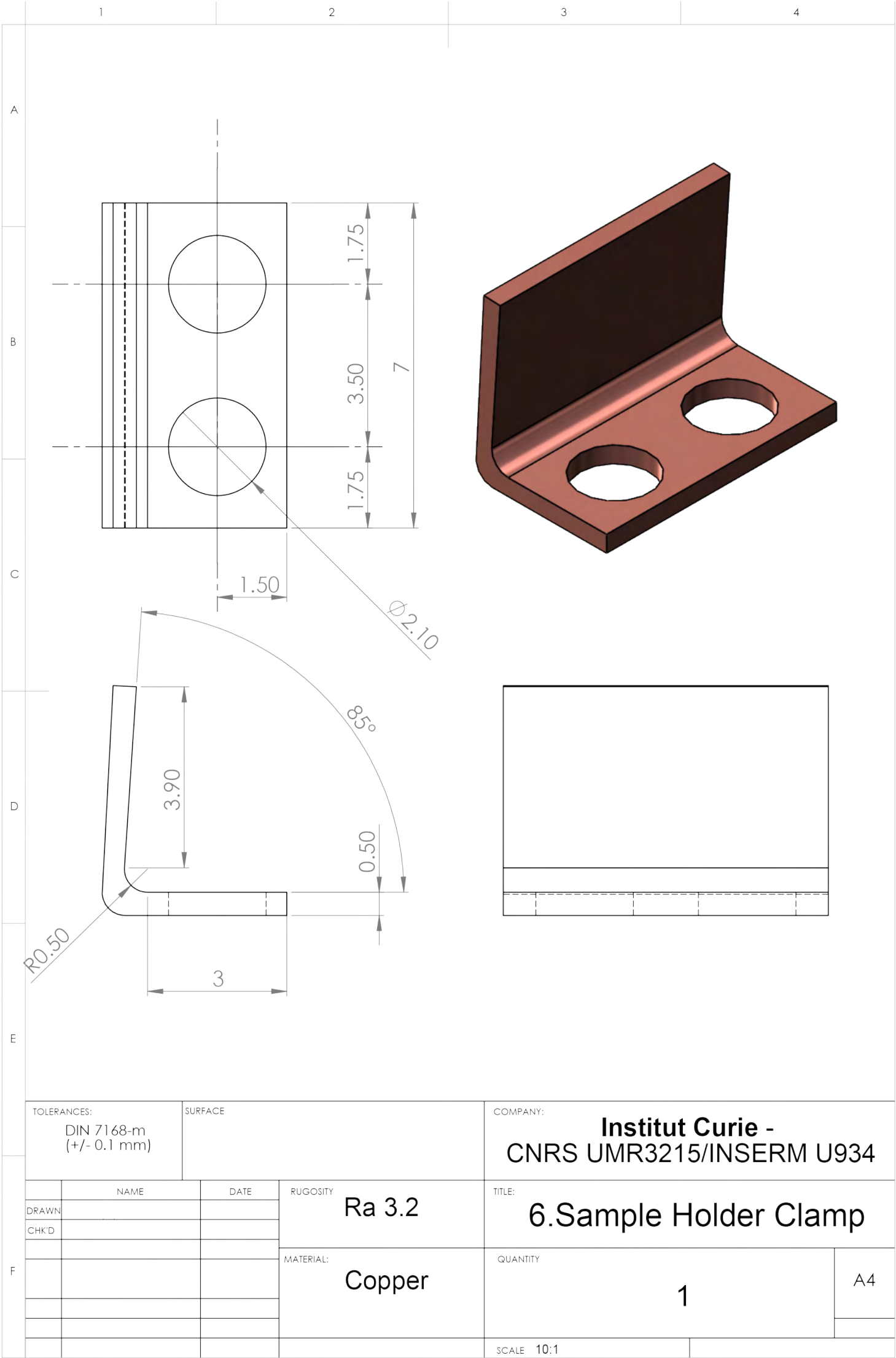


Fig. S2. Blueprint of the Multi-View confocal microScope (MuViScope).

A) Schematic illustration of the MuViScope showing the complete instrument that has been divided in eight blocks: (1) Camera and Spinning head, (2) Relay lens system, (3) Motorized flip mirror, (4) Right arm, (5) Left arm, (6) Specimen-positioning system, (7) Temperature and humidifier, (8) Computer and software.

B) List of the optical elements, the opto-mechanical and the mechanical components used to mount the MuViScope.

C) Technical drawings of the custom-made components: (Block 3) Scanner body, mirror body and mirror of the flip mirror; (Blocks 4 and 5) Adapters from SYS65 to SM2 and from SYS65 to SM1ZP; (Block 6) Adapters from M404 to M111, from M111 to M660 and from M660 to Sample Holder, Sample Holder and Clamp.

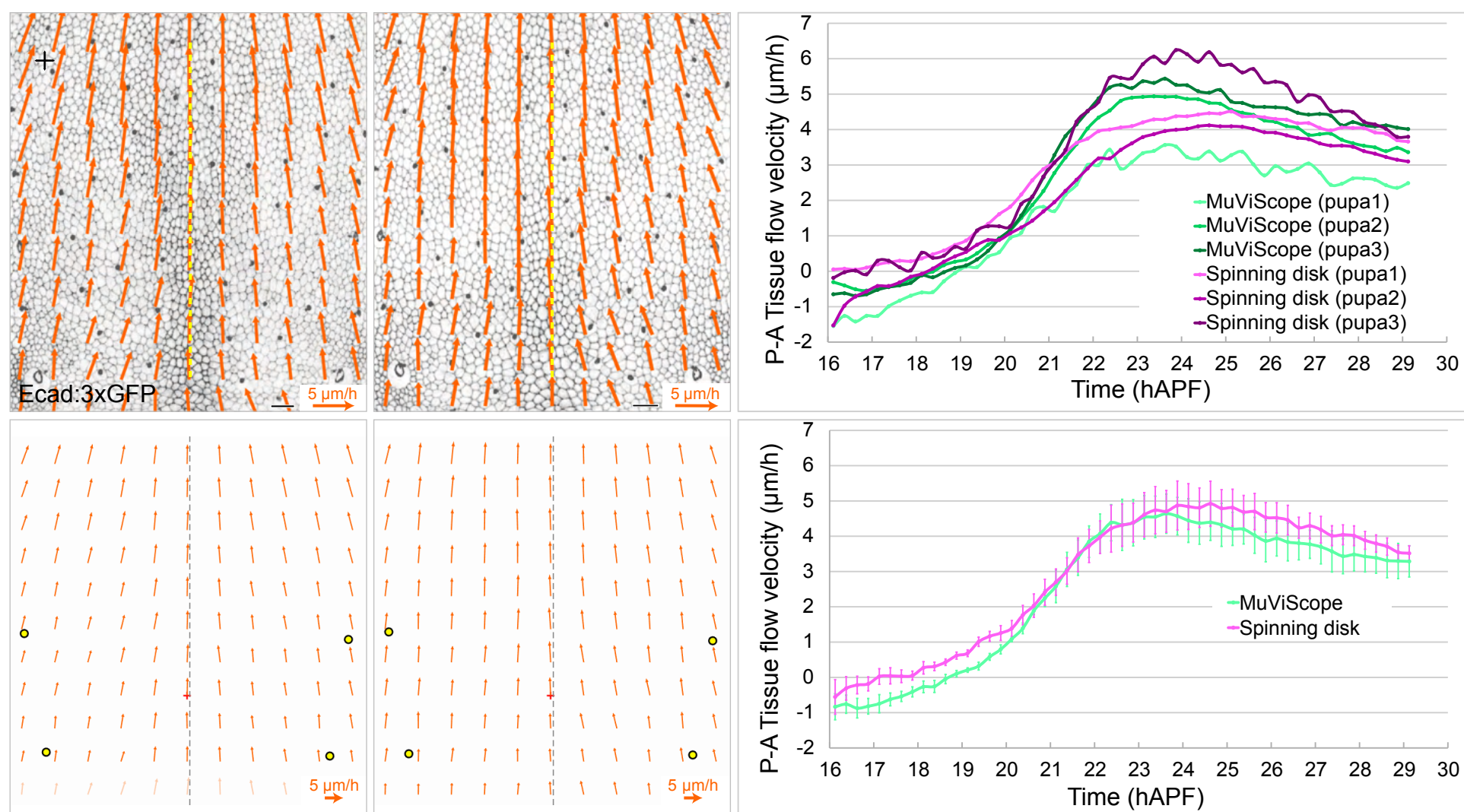


Fig. S3. Comparison of tissue flows in the notum of *Ecad:3xGFP Drosophila* pupae imaged using MuViScope or spinning disk microscopy.

Tissue flows were measured by PIV in the anterior notum (scutum) of *Ecad:3xGFP Drosophila* pupa by MuViScope (A, C, D, F) or by Spinning disk microscopy (B, C, E, F) between 16h and 29 hAPF using 40x magnification. The A-P and L-R axes are

indicated on the dorsal view in A. The midline is indicated by a yellow (A, B) or grey (D, E) dashed line. The barycenter is indicated by a red cross (D, E).

(A-B) Tissue flow maps between 24 and 26 hAPF for one *Ecad:3xGFP* expressing pupa imaged by MuViScope (A) or spinning disk microscopy (B).

(C) Graph of P-A tissue flow velocity for three pupae imaged by MuViScope (light green, green and dark green curves) and for three pupae imaged by spinning disk microscopy (pink, purple and violet curves) as a function of developmental time.

(D-E) Average tissue flow maps between 24 and 26 hAPF for three pupae imaged by MuViScope (D) or spinning disk microscopy (E). The macrochaetae used for registration are shown as yellow dots. The red cross indicates the barycenter between the macrochaetae.

Note that the flow is directed towards the anterior part of the scutum at this stage as previously described (Bosveld et al., 2012; Guirao et al., 2015).

(F) Graph of the mean (\pm sd) P-A tissue flow velocity for three pupae imaged by MuViScope (light green) and spinning disk microscopy (pink) as a function of developmental time.

The acquisition parameters are detailed in Table S1. Flow scale bar: 5 $\mu\text{m/h}$. Scale bars: 20 μm .

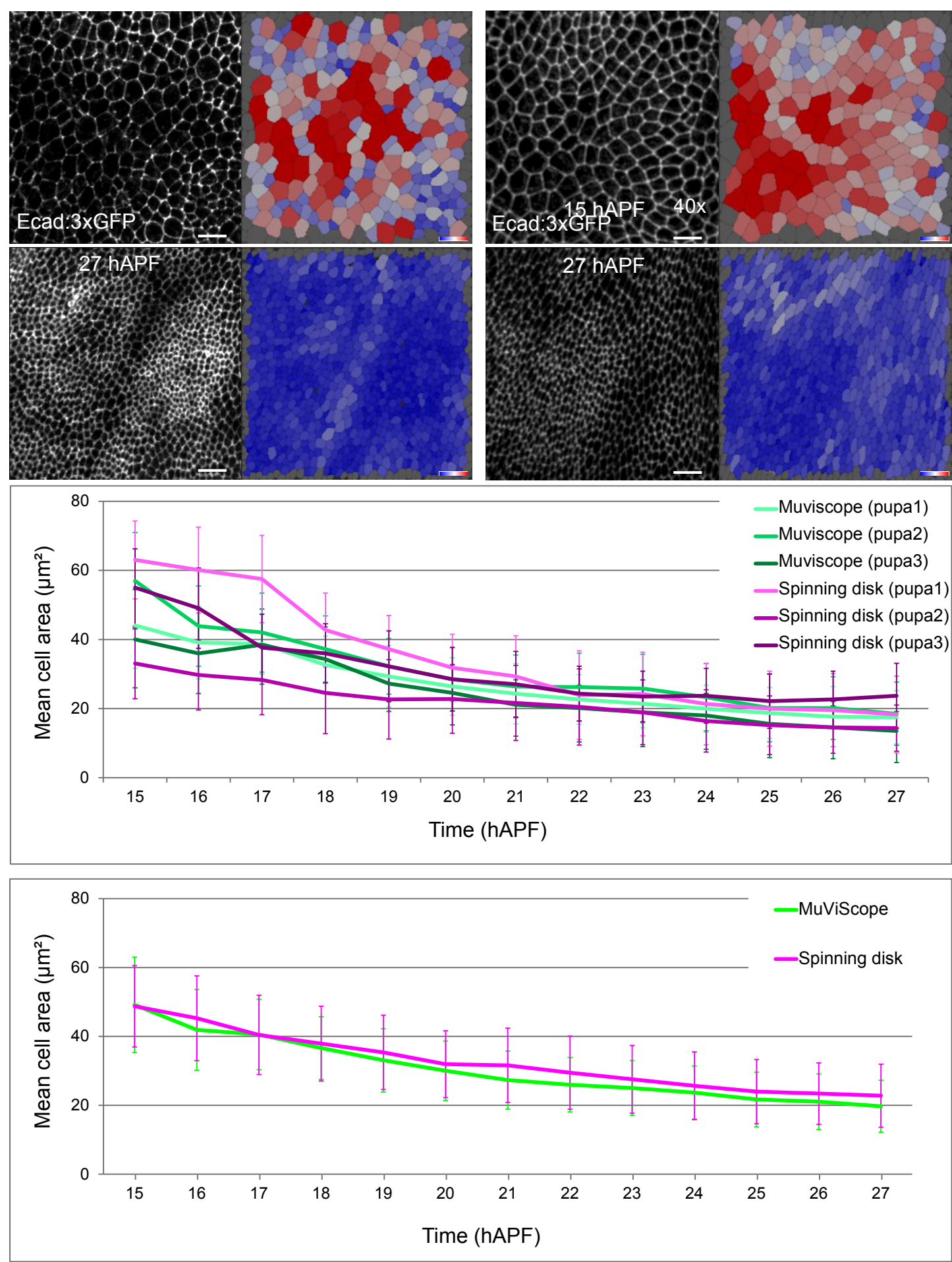


Fig. S4. Quantification of wing hinge apical cell area changes upon spinning disk microscopy and MuViScope.

Time-lapse images and quantification of apical cell area of Ecad:3xGFP wing hinge images either acquired by MuViScope (A, B, E, F) or spinning disk microscopy (C, D, E, F) or at 40x magnification.

(A, C) Maximum projection of time-lapse images of the *Drosophila* pupa wing hinge at 15 hAPF and 27 hAPF.

(B, D) Cell segmentation of time-lapse images with a color-coded (blue to red) representation of the apical cell area (from 5 to 100 μm^2).

(E) Graph of the average cell area (mean \pm sd) for 3 pupae imaged by spinning disk microscopy (pink curves) and MuViScope (green curves).

(F) Graph of the cell area averaged (mean \pm sd) over the 3 pupae in each imaging conditions. The area of cells decreases between 15 hAPF and 27 hAPF in both imaging conditions ($n=3$). The acquisition parameters are detailed in Table S1. Scale bar 10 μm .

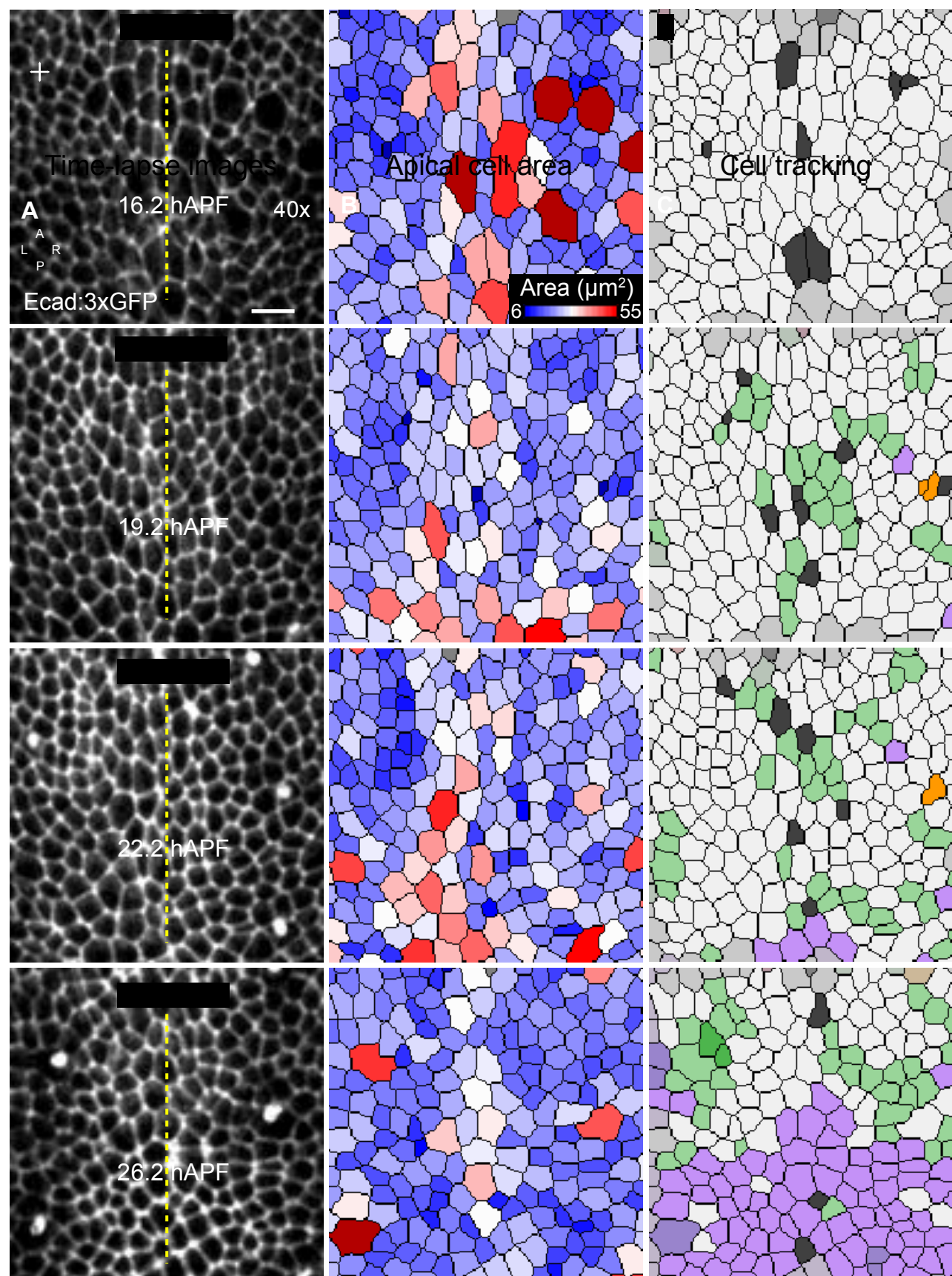


Fig. S5. Cell segmentation and tracking of the *Drosophila* pupa notum imaged by MuViScope.

Cell segmentation and tracking using time-lapse images of the dorsal view of an Ecad:3xGFP pupa imaged using the MuViScope at 40x magnification between 16.2 and 26.2 hAPF. The A-P and L-R axes are indicated in A. The dotted line indicates the position of the midline. A) Maximum projection of time-lapse images of the *Drosophila* pupa notum at indicated developmental time points.

B) Cell segmentation and quantification of apical cell area by a color code (blue to red) for the images shown in A.

C) Cell tracking of the tissue imaged in A. The color code is as follows: green, cells having undergone one cell division; purple, cells that were not in the field of view at t=16.2 hAPF due to the posterior to anterior flow of notum cells; dark grey, cells that will delaminate at a later time point; orange, cells originating from a segmentation error producing a false cell division; gray, border cells that were not tracked. Image collection was performed at 40x without tiling.

The acquisition parameters are detailed in Table S1. Scale bar 10 μm.

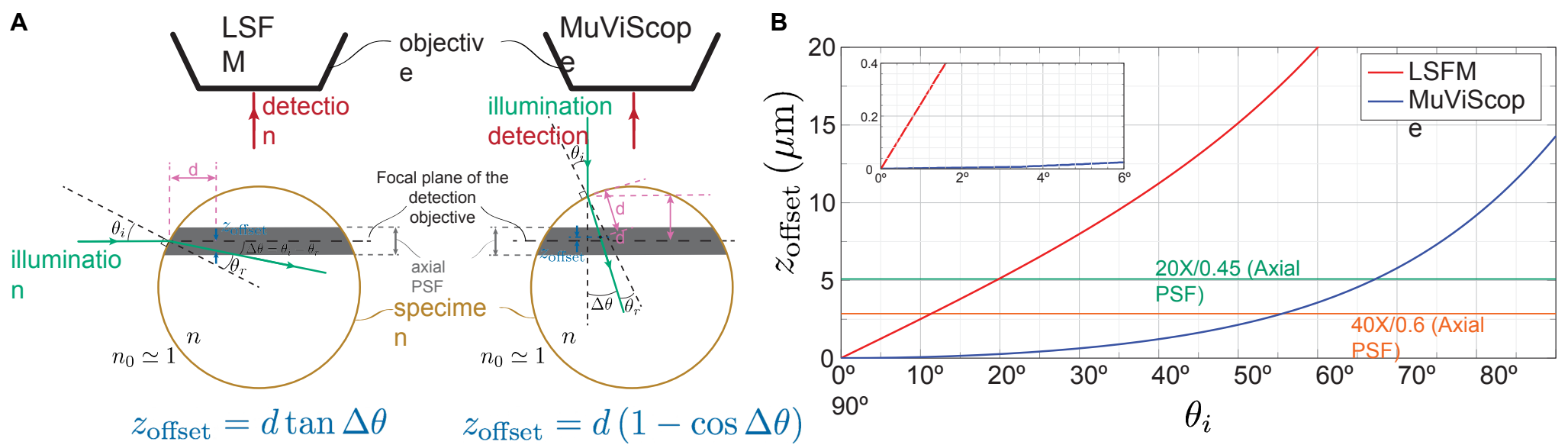


Fig. S6. Theoretical representation of illumination excitation between LSFM and MuViScopy depending on the angle of incidence for non-immersed condition.

(A) Diagram showing the theoretical illumination light path using LSFM (left) and MuViScopy (right) in non-immersed conditions. When the specimen is imaged in air conditions, the excitation light beam (in green) that hits the air/specimen interface at an oblique incidence is deflected due to the RI mismatch between the air ($n_0 \simeq 1$) and the specimen (n within the range of 1.38 – 1.42). This usually results in spherical aberrations that misalign the optical paths and attenuate the image quality (Booth and Wilson, 2001). For a sample with a constant RI, the main effect is a z -offset of the illumination focal plane of $d \tan(\Delta\theta)$, for LSFM whereas the z -offset only scales with $d[1 - \cos(\Delta\theta)]$ in the case of MuViScopy (with d the sample depth, $\Delta\theta = \theta_i - \theta_r$ the difference between the angles of incidence θ_i and refraction θ_r with $\theta_r = \arcsin\left(\frac{\sin \theta_i}{n}\right)$ given by the Snell-Descartes law.

(B) Plot of the z -offset as a function of the angle of incidence for LSFM (red) and MuViScopy (blue). Theoretical axial resolution of objective 20x/0.45NA (green line) and 40x/0.6NA (orange line) are also plotted. For example, for a θ_i of 20° and a depth of $50 \mu\text{m}$, the z -offset will be in the order of $5.13 \mu\text{m}$ for the LSFM and $0.26 \mu\text{m}$ for the MuViScopy. Insert: close-up for θ_i below 6° . Under these conditions (non-immersed sample) MuViScopy perform better than LSFM.

Table S1. Table summarising the acquisition parameters of the figures and movies.
Leroy et al

Figure #	Sample type	Stage	Marker	Microscope type	Live/dead/fixed	Dry/immersed sample	Temperature (°C)	Magnification(s)	Exp. Time (ms)	Laser power	Dimension	Nb z-slices	z-step (µm)	z-Max (µm)	Nb of positions	Nb of angles	Nb of angles shown	angle (degrees)	Time-lapse duration	Time between time-points	Comments
Figure 1	drosophila pupae	40xAPF	Ecad-3xGFP	LightSheet Z1	Dead	Immersed	RT	20x	100	50mW @ 488nm	xy-z--x	416	1.27	yes	8 (show only 4)	1	1	NA	NA	NA	Dual side excitation and dual side fusion
Figure 2AB	drosophila pupae	31xAPF	Ecad-3xGFP	PhaseView Alpha 3	Live	Dry	RT	10x	200	50mW @ 488nm	xy-z--y	331	2	yes	1	2	2	90°	NA	NA	Dual side excitation, manual rotation
Figure 2CD	drosophila pupae	30xAPF	Ecad-3xGFP	MuViScope	Live	Dry	25	10x	400	150mW @ 488nm	xy-z--y	318	2	yes	1	2	2	90°	NA	NA	
Figure 2FG	drosophila pupae	31xAPF	Ecad-3xGFP	MuViScope	Live	Dry	25	10x and 40x	400	150mW @ 488nm	xy-z--M	75 (10x), 100 (40x)	4 (10x), 2 (40x)	yes	1	1	1	NA	NA	NA	2 magnifications (10x and 40x)
Figure 4A	drosophila pupae	pharate	Ecad-3xGFP	MuViScope	Live	Dry	25	10x	400	150mW @ 488nm	xy-z--y	100	4	yes	1	361	5	0/20/40/60/90°	NA	NA	
Figure 4B	Kranus	adult	no marker	MuViScope	Dead	Dry	RT	10x	400	150mW @ 488nm	xy-z--y	200	4	yes	1	360	7	1°	NA	NA	auto fluorescence
Figure 4C	Tribolium	adult	atub1-LikeAct:GFP, EF1a-nls:GFP A	MuViScope	Dead	Dry	RT	10x	400	150mW @ 488nm	xy-z--y	100	10	yes	3	12	6	60°	NA	NA	
Figure 5	drosophila pupae	6-97hAPF	hh-DelRed	MuViScope	Live	Dry	25	10x	400	150mW @ 561nm	xy-z--y	100	5	yes	2	4	4	90°	91h	15min	
Figure 6	drosophila pupae	25-68hAPF	Mz2-COR:GFP	MuViScope	Live	Dry	25	10x	400	150mW @ 488nm	xy-z--y	101	4	yes	1	3	3	0/90°/180°	2h	24h	
Figure 7A	drosophila pupae	16-37hAPF	Ecad-3xGFP	MuViScope	Live	Dry	25	10x	400	150mW @ 488nm	xy-z--y	75	4	yes	1	2	2	90°	21h	10h	
Figure 7B	same sample as 7A			MuViScope	Live	Dry	25	40x	400	150mW @ 488nm	xy-z--x	100	2	yes	2	1	1	NA	21h	10h	
Figure 7C	drosophila pupae	16-37hAPF	Ecad-3xGFP, dpy ²⁰¹	MuViScope	Live	Dry	25	10x	400	150mW @ 488nm	xy-z--y	75	4	yes	1	2	2	90°	21h	10h	
Figure 7D	same sample as 7C			MuViScope	Live	Dry	25	40x	400	150mW @ 488nm	xy-z--x	100	2	yes	2	1	1	90°	21h	10h	
Movie 2	Tribolium	adult	atub1-LikeAct:GFP, EF1a-nls:GFP A	MuViScope	Dead	Dry	RT	10x	400	150mW @ 488nm	xy-z--y	100	10	yes	3	11	11	30°	NA	NA	
Movie 3	drosophila pupae	0.5-97hAPF	hh-DelRed	MuViScope	Live	Dry	25	10x	400	150mW @ 561nm	xy-z--y	100	5	yes	2	4	4	90°	96.5h	15min	
Movie 4	drosophila pupae	25-68hAPF	Mz2-COR:GFP	MuViScope	Live	Dry	25	10x	400	150mW @ 488nm	xy-z--y	101	4	yes	1	3	3	90°	2h	4h	
Movie 5	drosophila pupae	16-37hAPF	Ecad-3xGFP & Ecad-3xGFP, dpy ²⁰¹	MuViScope	Live	Dry	25	10x	400	150mW @ 488nm	xy-z--y	75 (10x), 100 (40x)	4 (10x), 2 (40x)	yes	2	2	2	90°	21h	30min	Some data used for Fig1 with Fusion/deconvolution of 4 angles
Figure S1	drosophila pupae	34hAPF	Ecad-3xGFP	LightSheet Z1	Dead	Immersed	RT	20x	100	50mW @ 488nm	xy-z--y	416	1.27	yes	8 (show only 4)	4	1 (fusion + deconvolution)	0/90°/180°/270°	NA	NA	
Figure S2	drosophila pupae	24h-35hAPF	Ecad-3xGFP	MuViScope	Live	Dry	25	40x	400	150mW @ 488nm	xy-z--x	151	4	yes	1	1	1	NA	2h	15min	PRV - see full movie S4
Figure S4	drosophila pupae	15-27hAPF	Ecad-3xGFP	Spinning disk	Live	Dry	25	40x	100	150mW @ 488nm	xy-z--x	40	1	yes	1	NA	NA	NA	2h	15min	PRV - see full movie S4
Figure S5	drosophila pupae	8-2-25hAPF	Ecad-3xGFP	Spinning disk	Live	Dry	25	40x	100	150mW @ 488nm	xy-z--x	26	0.5	yes	1	NA	NA	NA	12h	30min	Segmentation for cell area measurement
Movie S1	drosophila pupae	12-14hAPF	Ecad-GFP	Spinning disk	Live	Dry	25	40x	100	150mW @ 488nm	xy-z--x	26	0.5	yes	1	NA	NA	NA	15h	5min	Segmentation/tracking
Movie S2	drosophila pupae	28hAPF	Ecad-3xGFP	MuViScope	Live	Dry	25	10x	400	150mW @ 488nm	xy-z--y	151	4	yes	4	8	8	0/45/90°/135°/180°/225°/270°/315°	NA	NA	3D fusion reconstruction
Movie S3	drosophila pupae	34hAPF	Ecad-3xGFP	MuViScope	Live	Dry	25	40x	400	150mW @ 488nm	xy-z--y	151	4	yes	25 (5x5)	4	4	0/90°/180°/270°	NA	NA	3D fusion reconstruction
Movie S4	drosophila pupae	24hAPF	Ecad-3xGFP	MuViScope	Live	Dry	25	40x	400	150mW @ 488nm	xy-z--x	151	4	yes	1	1	1	NA	12h	15min	PRV

Abbreviations:
θ angle
M file
t time

Table S2. Performance comparison between light-sheet fluorescence microscopy and MuViScope in the context of *in-toto* live-imaging of non-immersed/non-embedded organisms

Non-Immersed Sample imaging		
	Light-sheet fluorescence microscope (LSFM)	Multi-View confocal microScope (MuViScope)
Excitation light efficiency ¹⁾	In focus plane	Entire specimen
Energy load (in air)/image ²⁾	++	++
Photobleaching	++	+
Lateral & axial resolution ³⁾ in air	low	++
Dynamic range	++	+
Imaging Speed	++ Few 10's of ms using CMOS camera	++ Few 100's of ms using CMOS camera
Multiview imaging and deconvolution-fusion	++	++
Simultaneous multiple magnifications ⁴⁾	- (commercial)	++
Cost efficiency	~100 k€ (home-made) ~300 k€ (commercial)	~200 k€ (home-made)

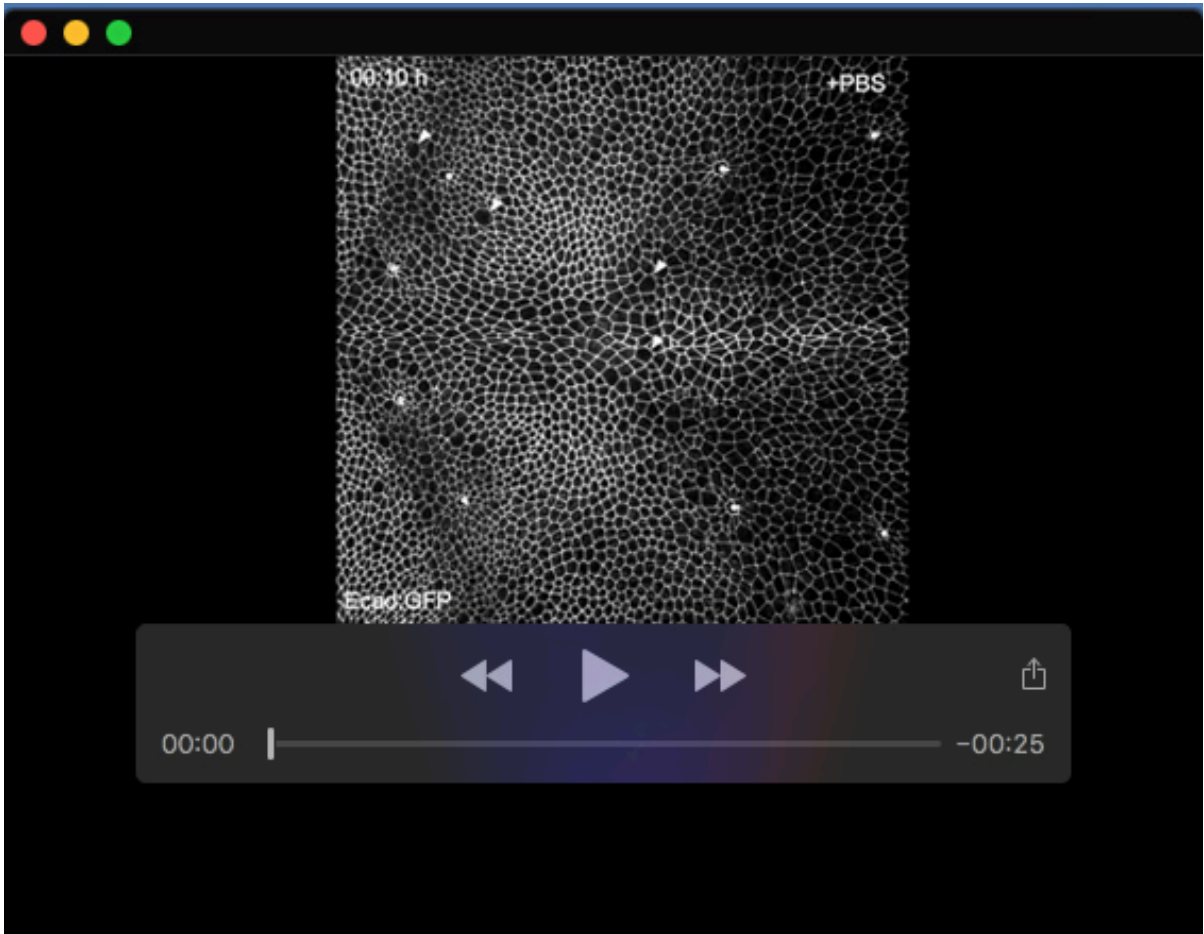
++ good performance, + medium performance, - low performance

¹⁾ i.e., efficiency in using illumination light exclusively for fluorescence excitation in the focal plane of the detection lens.

²⁾ Power measurement at the back focal plane of the objective: 6 mW (PhaseView) and 0.6 mW (MuViScope) with the exposure time to acquire one image 10 times higher for the MuViScope (see row “Imaging Speed”). The energy is about 60 µJ/image for both systems.

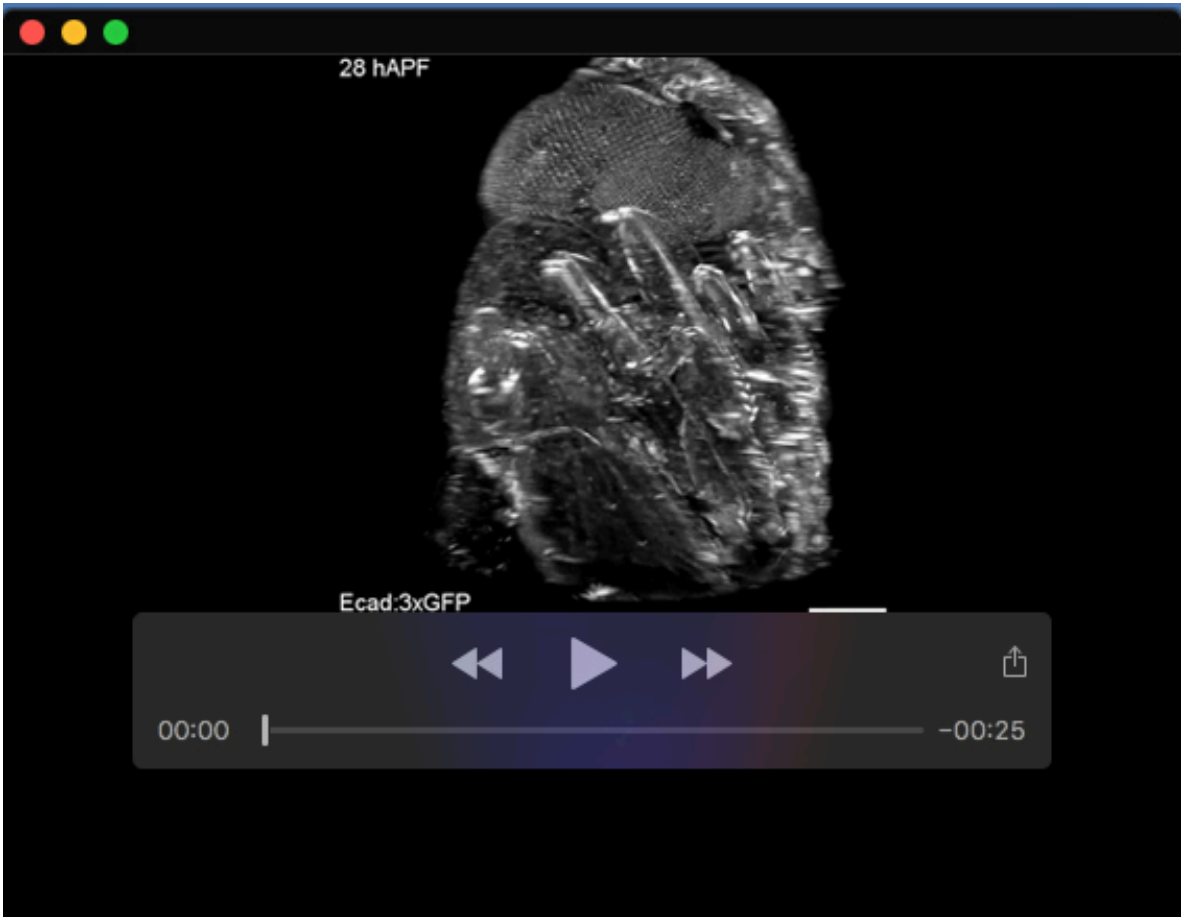
³⁾ Not considering image deconvolution. Exact values depend on the choice of objective. The axial resolution is equivalent to lateral resolution in Multiview imaging for both systems.

⁴⁾ The MuViScope can be equipped with two objectives with different magnifications at opposite sides of the sample, which allows simultaneous imaging of the sample at medium (20x or smaller) to high (40x or higher) magnifications. To our knowledge there is no commercial light-sheet microscope that permits mounting of two detection objectives with different magnifications.

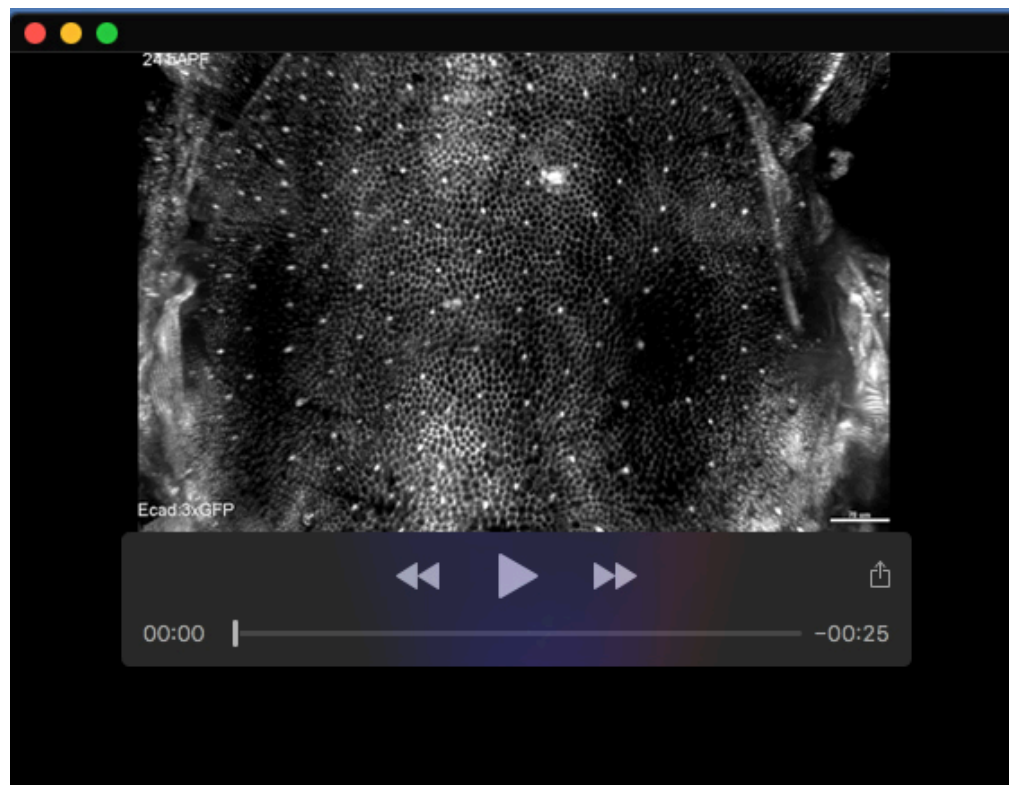


Movie 1. Spinning disk time-lapse imaging of a pupa with and without immersion in PBS.

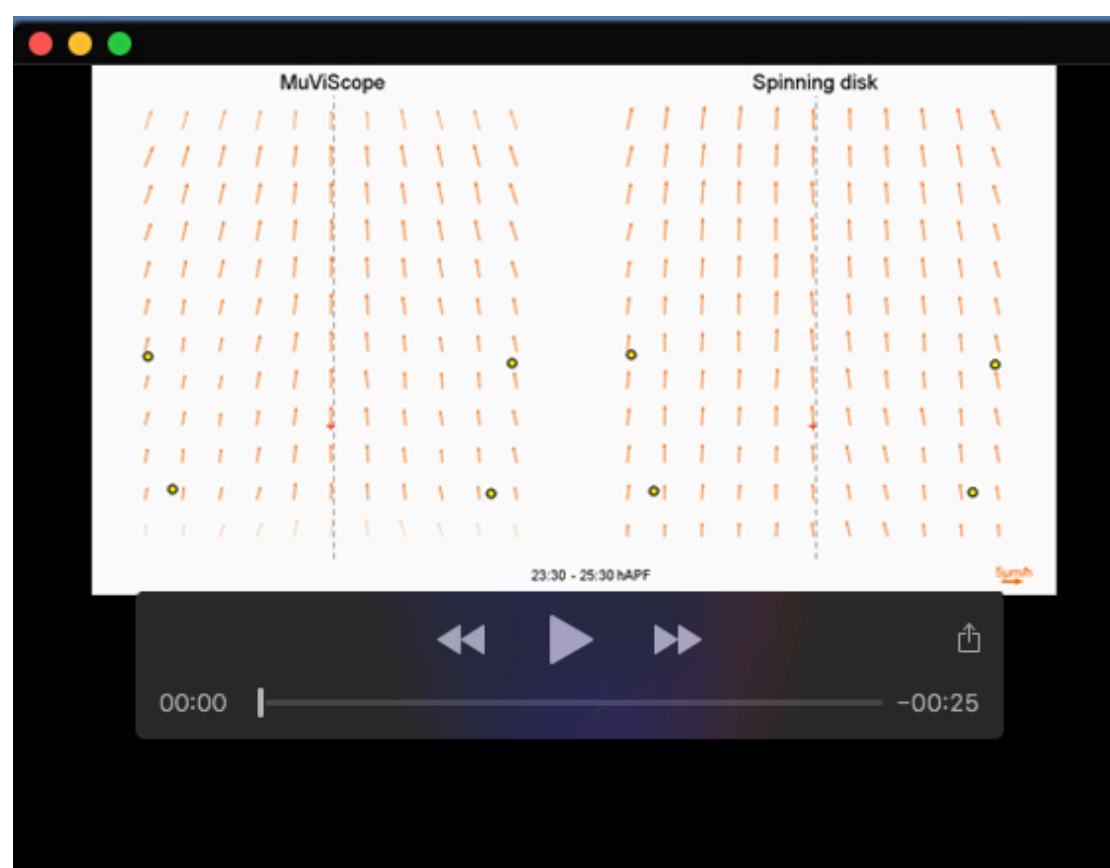
A 12 hAPF pupa expressing Ecad:GFP was mounted under a coverslip and imaged by spinning disk microscope for 50 min before adding PBS (t=0). Cell divisions can be observed throughout the tissue before PBS addition. Cells in metaphase at t=0 min do not complete mitosis (arrowheads). The acquisition parameters are detailed in Table S1. Scale bar: 50 μ m.



Movie 2. 3D fusion reconstruction of 8 different angles at 10x magnification. Animation of a 3D reconstruction after fusion of images acquired from 8 angles by the MuViScope of an Ecad:3xGFP *Drosophila* pupa at 28 hAPF with a 10x objective. The animation starts with a 180° rotation along the A-P axis and then sequentially shows the 8 different angles from a top view: 0° (red), 45° (orange), 90° (yellow), 135° (green), 180° (light blue), 225° (dark blue), 270° (purple) and 315° (pink). Fusion was performed using Huygens Fuser (SVI) and 3D visualization with Imaris software. The acquisition parameters are detailed in Table S1. Scale bar: 200 μ m.



Movie 3. 3D fusion reconstruction of 4 different angles at 40x magnification. Animation of a 3D reconstruction after fusion of images acquired from 4 angles (0° , 90° , 180° and 270°) by the MuViScope of an Ecad:3xGFP *Drosophila* pupa at 24 hAPF with a 40x objective to achieve cellular resolution. At each angle, 25 tiles (5x5) were acquired to cover the full dissected part of the animal. Each tile was then deconvolved with the Huygens software and then stitched with the Pairwise Stitching plugin (Preibisch et al., 2009). The animation starts with a dorsal view of the notum and the head, followed by a zoom cellular resolution on the notum and finishes by a 360° rotation around the A-P axis. The acquisition parameters are detailed in Table S1. Scale bar: indicated on the film according to the zoom factor (in μm).



Movie 4. Comparison of average tissue flow during pupal development upon acquisition by MuViScope or spinning disk microscopy.

Average tissue flow between 17 – 26.45 hAPF in the dorsal thorax epithelium of *Drosophila* pupae Ecad:3xGFP imaged by MuViScope ($n=3$) or spinning disk microscopy ($n=3$) using a 40x objective. The averaged movies were generated upon time-lapse movie registration and rescaled using the macrochaetae (yellow dots). The red cross indicates the barycenter between the macrochaetae. The midline is indicated by a grey dashed line. Tissue flow is quantified by velocity vectors measured by PIV (Guirao et al., 2015) and averaged over 2 h. The scale bar represents a displacement of $5 \mu\text{m/h}$.

Material S1: Leroy, van Leen *et al.*

Supplemental methods

Protocol for the preparation of Drosophila pupa for imaging using the MuViScope

1. Materials:

- *Drosophila* stock
- Temperature incubator
- Petri dish
- Precision wipes Kimtech Science (Kimberly-Clark Professional) or another brand
- Capillary tube 20 μ l (Brand #701904)
- Home-made metal rod with a flat platform (same length and diameter as 20 μ l capillary tube)
- Dental glue 3M ProTemp II (3M #46090)
- Double-sided tape 3M (3M#D6661933)
- Pair of forceps and micro-scissors
- 100 μ l pipette cone
- MuViScope capillary holder

2. Method:

Day 1:

- Collect white pupae (0 hAPF) and place them in a petri dish with moistened precision wipes paper.
- Put the dish in an incubator at 25°C.
- Leave the pupae in the incubator for the time of development (e.g.: 15 h for imaging at 15 hAPF).

Day 2:

- Turn on the temperature incubator of the MuViScope and set it to 25°C with a low speed fan.
- Fill the humidifier tank and turn it on. It should be set to 70-80% humidity with low speed fan.
- Take the pupae out of the incubator at the desired time and select a pupa.



- Let the pupa dry for 1-2 min on a precision wipe.

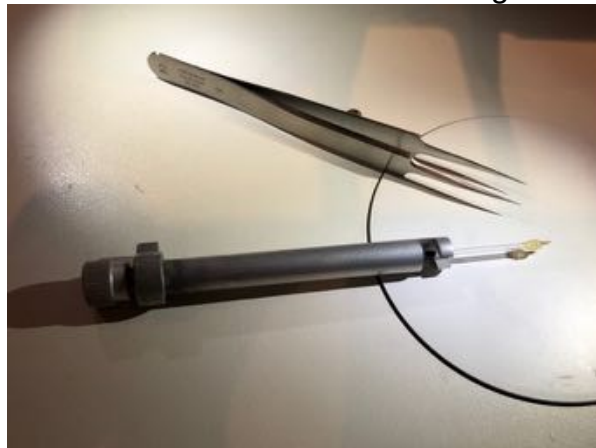
Option 1: Dental glue mounting (for 360° imaging).

- Prepare the dental glue ProTemp II according to the manufacturer's instructions.

- Use a 100 μ l cone to take a small amount of the mixture and place it on the end of the 20 μ l capillary tube. A small amount is sufficient.



- Insert the capillary into the capillary holder of the MuViScope.
- Under a binocular, take the pupa carefully with a pair of forceps and place its posterior part on the glue on the end of the capillary. Make sure the pupa is centered with the tube and in alignment with the tube.



- Wait for the dental glue to dry.



- When the glue to dry.

Option 2: Double-side tape mounting (for 180° imaging).

- Insert the home-made metal rod with a flat platform into the capillary holder of the MuViScope.
- Stick the double-sided tape on the platform and cut it to size.

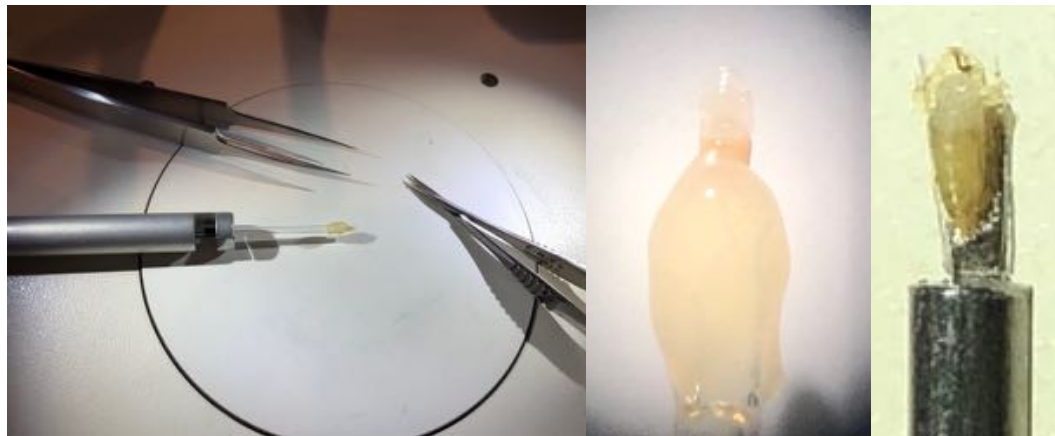


- Under a binocular, take the pupa carefully with a pair of forceps and stick it on the tape lengthwise with the head towards the end.

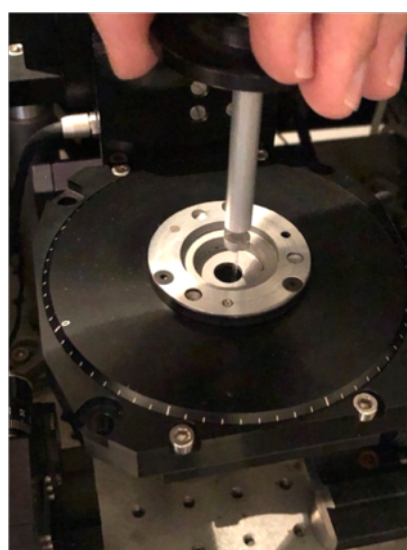


Dissection and mounting on the MuViScope:

- Start the dissection of the pupa under the binocular using the forceps and the dissecting scissors as described in Zitserman et al. (Jauffred and Bellaiche, 2012; Zitserman and Roegiers, 2011).
- With one hand hold the capillary holder under the binocular and with the other hand start removing the pupa operculum. Then with the scissors cut the pupal case lengthwise from the anterior to the posterior part along the wing. Remove the pieces of the pupal case with forceps. The middle picture shows a pupa fixed with dental glue and dissected while the right picture shows a taped and dissected pupa. The magnifications of the photos are not identical.



- Then place the MuViScope capillary holder with dissected pupa on the rotating stage of the MuViScope.



- Focus on the sample and set the acquisition parameters of the MuViScope.
- Start image acquisition.

Bibliography:

Jauffred, B. and Bellaiche, Y. (2012). Analyzing frizzled signaling using fixed and live imaging of the asymmetric cell division of the *Drosophila* sensory organ precursor cell. *Methods in molecular biology (Clifton, N.J.)* **839**, 19–25. **Zitserman, D. and Roegiers, F.** (2011). Live-cell Imaging of Sensory Organ Precursor Cells in Intact *Drosophila* Pupae. *JoVE (Journal of Visualized Experiments)* e2706.